Available online at www.sciencedirect.com
SCIENCE DIRECT®
Journal of Sound and Vibration 273 (2004) 875–919
JOURNAL OF SOUND AND VIBRATION
www.elsevier.com/locate/jsvi

Dynamic characteristics of a flexible bladed-rotor with Coulomb damping due to tip-rub

S.K. Sinha*

G.E. Aircraft Engines, General Electric Company, 1 Neumann Way, Cincinnati, OH 45215, USA

Received 17 July 2002; accepted 12 May 2003

Abstract

Starting with the basic dynamical equations for a rotating radial cantilever blade in a centrifugal force field, a system of equations are derived for a fully-bladed flexible rotor (shaft and disk) supported by a set of bearings at multiple locations. The dynamical equations include the effect of the rotary inertia and gyroscopic moments as a result of both shaft bending as well as staggered blades flexing in-and-out of the plane of the disk. The governing equations also account for internal material damping in the shaft and the external damping in the bearing. In addition to the unbalance load at the disk location, the shaft may be subjected to a torque and axial forces. In the analytical derivation, the blade tips are considered to be rubbing against the outer case introducing Coulomb damping in the system. Transient response of the rotor with the blades deforming due to rub during the acceleration and deceleration through the resonance is discussed. Numerical results are presented for this highly non-linear impact dynamics problem of hard rub with Coulomb friction. The effect of blade tip rub forces transmitted to the shaft are analyzed in terms of the dynamic stability of the rotor.

1. Introduction

In any high-performance turbo-machinery, rub is a commonly occurring problem. Higher energy-efficiency of the engine is achieved by reducing the tip clearance between the rotor and the stator components, but as the clearance is reduced; the probability of rub taking place during small changes in the operating conditions also increases. It is known that the rub forces can be extremely high causing severe damage, but due to the short duration involved, determining its true magnitude has been a real challenge. Rubbing of rotating blade tips against the stationary outer

*Tel.: +1-513-243-3200; fax: +1-513-243-8091.
E-mail address: sunil.sinha@ae.ge.com (S.K. Sinha).

0022-460X/$ - see front matter © 2003 Elsevier Ltd. All rights reserved.
doi:10.1016/S0022-460X(03)00647-3

case is a highly non-linear contact–impact event, and until now no one has attempted to solve it analytically, covering its full dynamic characteristics.

In a jet engine high-pressure compressor and fan, the case distortion can also result in a blade or a sector of blades rubbing against the case. Specifically, in aero-engines, the case distortion may be caused either by a temperature gradient or due to various maneuvering loads usually during take-off and landing of the aircraft. Unbalance forces can also start the blade tip-rub which may be caused either by damage to the fan blade due to bird-strike or, due to sudden blade loss as well. Dynamic response of blade and containment case during rub is greatly influenced by the amount and nature of damping present in the system. Consideration of damping is an important aspect in analyzing the dynamic characteristics of the blade–case interaction. The damping can be present both as an internal damping due to material friction such as in viscoelasticity in the shaft and blade material as well as external damping such as Coulomb friction at the blade-tip or other joints and in the support system. The non-conservative nature of the damped system introduces many complexities in the analysis [1], which one usually gets around by making several simplifying assumptions. For instance, decoupling the equations of motion with non-uniform damping by modal analysis [2,3] is one approach. In the finite-element method, it is a common practice to represent the damping matrix [**C**] as a linear combination of the mass matrix [**M**] and the stiffness matrix [**K**] as

$$[\mathbf{C}] = \alpha[\mathbf{M}] + \beta[\mathbf{K}].$$

The above assumption makes it difficult to analyze the effect of gyroscopic terms in a rotating system, where the [**C**] matrix is in fact skew-symmetric. In this paper, we consider the dynamic stability of a complete rotor system in a jet engine with its blade rubbing against the containment case. Here, by using Galerkin's method a direct matrix formulation of the non-linear dynamic problem has been developed, which does not make any such simplifying assumptions, nor does it need any transformation. Yet, it is general enough to include the effect of viscoelasticity, non-uniform support damping as well as the gyroscopic terms. This paper analyzes the effect of internal damping on the dynamic stability of an overhung rotor supported by a set of bearings at multiple locations and deformable blades rubbing against a case at the other end (see Fig. 1). The rotor shaft may be under a periodic sinusoidal axial force superimposed on a constant static axial load and torque on the system. In a rotating machinery, such pulsating axial forces are usually caused by misalignment. The rotor system considered in this paper is composed of a flexible hollow shaft, a rigid disk, and a full set of flexible blades, a sector of which may be rubbing against an elastically deformable outer surface. In this study, we consider two types of contact with the outer containment surface: (1) the outer surface behaves like a rigid wall and the spinning shaft–disk with bladed rotor as an impactor; (2) the inner surface of the outer case has a lining of a relatively soft material like honeycomb, foam or, an abradable coating against which the blade tip is allowed to rub.

The Coulomb friction between the blade tip and the outer surface introduces skew-symmetric terms in the stiffness matrix for the rotor shaft, which, depending upon the amount of effective damping present in the dynamical system, can initiate instability in the bladed-rotor shaft.

In rotordynamics, due to complexity of the non-linear analysis, the flexible shaft–disks of the dynamical system are frequently reduced to much simplified two-degrees-of-freedom rotor models made up of a set of lumped-masses and springs. Furthermore, due to large computation time

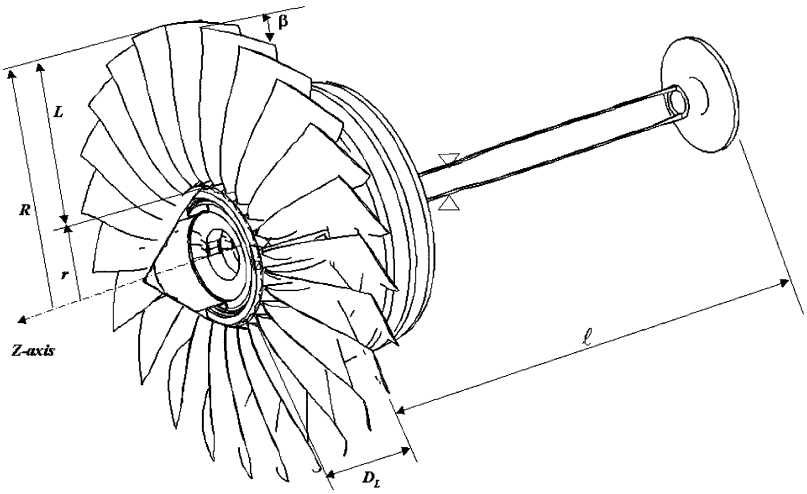

Fig. 1. A typical fan rotor in a jet engine with hollow shaft: outside radius $= r_o$, inside radius $= r_i$.

involved, an attempt is usually made to obtain the solution only in the frequency domain, where peak responses are determined at certain pre-determined harmonic excitation frequencies. Then, transient response is computed by multiplying the harmonic response by a factor called "transient overshoot factor". Among the notable contributions on this topic, Plaut [4] analyzed the stability of a simply-supported rotating shaft with axial load and damping in the system. Cohen and Porat [5] used an asymptotic method to investigate the combination-resonance effect in coupled transverse vibration of an unbalanced rotor. Yim et al. [6] studied the destabilizing effect of tangential torque in the system. Sinha [7] established general conditions of rotordynamic stability, when oscillating axial forces are combined with the torque in the shaft. Recently, Lee and Yun [8] extended the stability conditions for three different types of end-conditions for the flexible shaft. The dynamical effect of rub-induced instability in the rotors was first studied by Child [9].

Until now, almost all the research work dealing with the Coulomb damping in a rotating system has been limited to the study of blades rubbing with different kinds of friction model. The macro-slip model for Coulomb friction between a stress-stiffened rotating turbine blade rubbing against a stationary surface has been used extensively by many researchers such as Sinha and Griffin [10]. Later on, Sinha [11] used a simple spring–mass system to calculate the optimal value of slip load for a frictionally damped turbine blade subjected to random excitation caused by a white noise. Wang and Shieh [12] determined the dynamic response of the rotating blades with velocity-dependent coefficient of friction. Sanliturk et al. [13] used a harmonic balance method to determine the amplitude-dependent complex stiffness of a friction damper to simulate damping in a turbine blade. Berger and his colleagues [14] have used a mixed differential algebraic equation approach to describe the slipping dynamics by differential equations and algebraic equations to represent the interfacial sticking during the rub action. It should be noted that all these damping models are relatively simple spring–mass system with a Coulomb-damper near the blade root with a ground-constraint. Choy, Padovan and their colleagues [15–17] have studied a true rotor–case rub phenomena and its effect due to friction in quite detail, however, they have neglected the

effect of stress stiffening of blades due to rotation, which is a major parameter in pulse buckling during rub.

The current paper analyzes the effect of a Coulomb-damper near the blade tip with the flexible blade mounted on a flexible rotating shaft. Starting from the basic beam equations along with the rotary inertia and gyroscopic effect terms, a complete set of coupled dynamic equations has been derived for this problem. The shaft with overhung disk can have multiple bearing support with varying amount of stiffness and damping in the x–y plane which are included in the equation by using the Dirac's Delta function.

2. Rotating cantilever beam formulation for flexible blades

Rotating turbine blade dynamics have been studied by several authors [18–21] in the past with different level of complexities such as from the lumped mass to the Timoshenko's beam formulation and large deformations of the free-end, etc. In this analysis, we consider that N-number of elastically deformable radial blades of outer radius 'R' with the stagger angle 'β' are mounted on a rigid disk. We will assume that the shaft stiffness at the center of the disk is 'K_{shaft}'. The blades behave like a cantilever beam–column of span length 'L' and are subjected to a centrifugal force field generated due to the rotor spin velocity 'Ω' with the blade tip rub load F_a acting along the beam axis. Thus, the lateral deflection in any typical jth blade with an in-plane force F_a (tension: + sign and compression: − sign) for a typical cross-section of the blade at a distance 's' from the root will be expressed as $\eta(s,t)$. The tip rub load F_a being a contact force between two bodies, is always compressive and is active only when the gap between the blade-tip and the outer case has closed. In other words, the non-zero value of F_a being compressive in nature will always have a negative sign (see Fig. 2a and 2b). Furthermore, it is assumed that the minor principal moment of inertia of the blade cross-section coincides with the chord direction so that under pure bending moment the blade lateral deflection $\eta(s,t)$ takes place in the direction normal to the chord with the neutral surface passing through the radial-chord plane. The equation of motion in a local frame of reference attached to the rotating blade for lateral deflection $\eta(s,t)$ from beam bending formulation can be written as

$$\begin{aligned}(EI)_b\eta_{,ssss} - (A)_b\sigma_{,s}\eta_{,s} - (A)_b\sigma\eta_{,ss} + (\rho A)_b\eta_{,tt} + C_t\eta_{,t}\delta(s-L) + K_{shaft}\eta\delta(s-0)\\ = \mu F_a\cos\beta\delta(s-L),\end{aligned} \tag{1}$$

where

$$\sigma(s) = \int_{s+r}^{R}(\rho)_b\Omega^2\xi\,\mathrm{d}\xi + \frac{F_a}{(A)_b} = (\rho)_b\Omega^2\frac{(R^2-r^2-2rs-s^2)}{2} + \frac{(F_a)_j}{(A)_b},$$

$$\frac{\partial\sigma(s)}{\partial s} = -(\rho)_b\Omega^2(s+r).$$

The blade material is also assumed to have its own internal damping the critical value of which is defined as

$$C_c = \frac{L^2}{\pi^2}[EI\rho A]^{1/2}_{blade}. \tag{2}$$

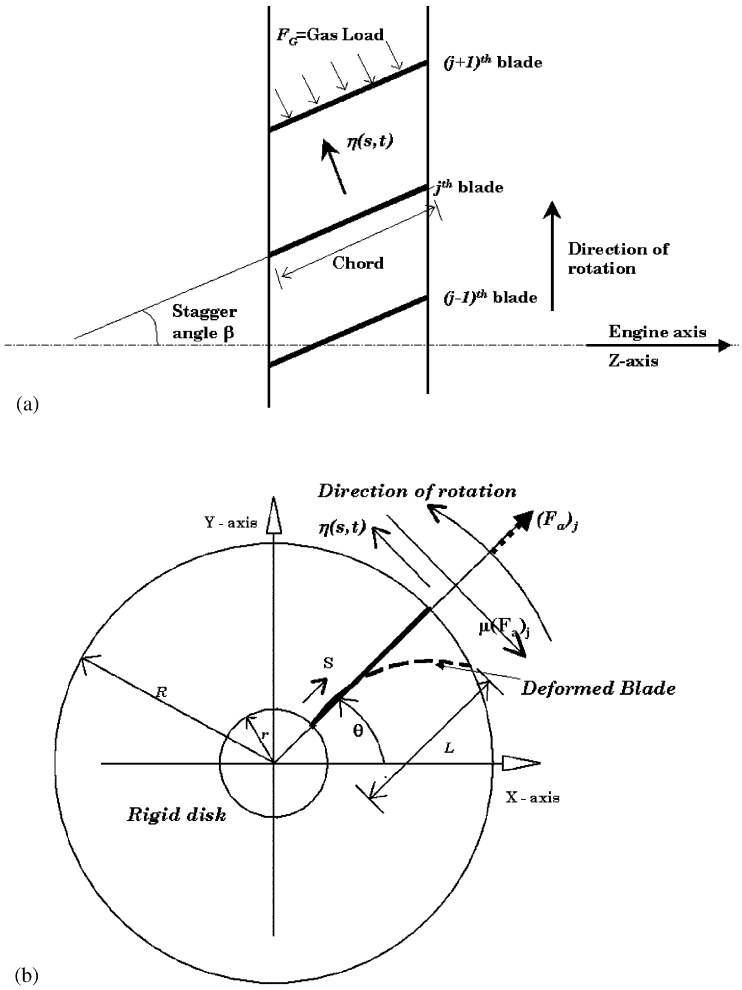

Fig. 2. (a) Top view of the cascade of fan blades: mass density $= (\rho)_b$, cross-sectional area $= (A)_b$, flexural rigidity $= (EI)_b$, Coulomb friction $= \mu(F_a)_j$. (b) Engine axis view of a typical blade deforming during rub.

For any viscous damping at the blade tip, it can be assumed that the viscous dash-pot at the blade tip exists with a non-dimensional damping factor 'ζ_b' which is a fraction of the critical damping parameter C_c defined earlier, such that

$$C_t = 2\zeta_b C_c.$$

If the outward radial movement of the blade tip exceeds the clearance with the outer case, a compressive force $(F_a)_j$ along its radial axis is applied, such that

$$\sum_{j=1}^{N} (F_a)_j \cos\left(\frac{2\pi j}{N} + \Omega t\right) = -(F_{case}(t))_X, \quad \sum_{j=1}^{N} (F_a)_j \sin\left(\frac{2\pi j}{N} + \Omega t\right) = -(F_{case}(t))_Y. \tag{3}$$

In the above equations, the vector sum of the radial contact load from the case '$F_{case}(t)$' is treated like a scalar and it is a function of time 't'. It should also be noted that F_{case} is always normal to

the inside surface of the containment ring. Thus in a full 360° uniform circumferential rub situation, for all blades $(F_a)_j$ will be non-zero, equal and compressive making the total sum of F_{case} equal to zero. In the more common type of rub event of a local contact in certain spots, F_{case} will have a non-zero value.

Being a compressive load along the typical jth blade-axis, $(F_a)_j$ has a set of critical values, which for a simple beam–column can be written as

$$(F_a)_j = -(EI)_b \left[\frac{(2n-1)\pi}{2L}\right]^2$$

where $n = 1, 2, 3, \ldots$ represent different buckled mode shapes.

In the static Euler's elastic buckling problem, this critical load is obtained by the lowest value of $n = 1$. However, in the transient dynamic situation of tip-rub, the suddenly applied axial load is many times greater than the static Euler load, causing the rotating blade to deform in higher modes. The beam–column can survive these large axial loads, if it is only for short duration, which is a typical scenario for a majority of the local rub in high-speed rotating machines [22]. Depending upon the damping and the coefficient of friction, certain conditions exist, when the rub will tend to destablize the rotor, and will send it either into backward or forward whirl. As mentioned earlier, in the present analysis, we assume a rigid case which can have a relatively soft filler material on its inside surface with a stiffness of K_{rub}. In a deformable outer case, the local rub generates a travelling wave with N_c number of diametral modes for the containment ring. Due to the travelling wave in the circumferential direction of the outer case, the net radial force from the case F_{case} would become a periodic force with a frequency '$N_c\Omega$' acting along the blade stacking axis, such that

$$F_{case} = F_{max} \cos(N_c \Omega t).$$

In this situation, the tip-rub load F_{case} may excite a 'N_c' number of nodal diametrical modes on the casing structure surrounding the rotating blades, the frequency of which may interact with the blade and rotor natural frequencies causing rub-induced resonance in the stator–rotor system. The periodic nature of the F_{case} turns the equation of motion for the blade into a classical Mathieu–Hill type of equation, showing the characteristics of parametric instability of the entire dynamical system.

The boundary conditions for each individual blades are

$$\eta(0, t) = 0, \quad \eta'(0, t) = 0, \quad EI\eta''(L, t) = 0$$

and, from the tip rub shear force at $s = L$,

$$EI\eta'''(L, t) - F_a\eta'(L, t) = \mu F_a \cos\beta.$$

Suppose, in the local co-ordinate system for the jth blade, the lateral deflection $\eta(s, t)$ is represented by the shape function

$$\eta(s, t) = (X_0(t))_j + \sum_{n=1}^{\infty} (X_n(t))_j (Y_n(s))_j. \tag{4}$$

Here, $(X_0(t))_j$ corresponds to the rigid-body displacement of the blade root caused by the transient movement of the disk, and $(X_n(t))_j \ldots$'s are the participation factors of individual mode-shapes in

determining the true deformed shape of the blade. Thus,

$$\eta(0,t) = (X_0(t))_j,$$

where

$$\eta(0,t) = \left[-u(\ell,t)\sin\left(\frac{2\pi j}{N} + \Omega t\right) + v(\ell,t)\cos\left(\frac{2\pi j}{N} + \Omega t\right)\right]\cos\beta,$$

$$(X_0(t))_j = \sum_{q=0}^{\infty}\left[-U_q(t)\sin\left(\frac{2\pi j}{N}\right) + V_q(t)\cos\left(\frac{2\pi j}{N}\right)\right]\cos\beta,$$

and where $U_q(t)$, $V_q(t)$ are the components of time-dependent displacement of the disk in the global x and y directions, respectively. The notations representing the shaft and disk deflection terms have been listed in Appendix A (Nomenclature), and are also explained in Eqs. (26) and (27). The deformed axial location of any point at radius 'r' on the blade with slope of the shaft at $z = \ell$ as φ_x and φ_y is given by

$$\begin{aligned}&\left[\varphi_x r\sin\left(\Omega t + \frac{2\pi j}{N}\right) - \varphi_y r\cos\left(\Omega t + \frac{2\pi j}{N}\right)\right] - (X_n(t))_j\sin\beta\\ &\quad= \left[(-v_{,z})|_{z=\ell} r\sin\left(\Omega t + \frac{2\pi j}{N}\right) - (u_{,z})|_{z=\ell} r\cos\left(\Omega t + \frac{2\pi j}{N}\right)\right] - (X_n(t))_j\sin\beta. \qquad (5)\end{aligned}$$

The axial movement of the blade introduces gyroscopic forces on the blade root, which is a velocity-dependent term. The magnitude of this axial velocity component is written as

$$\begin{aligned}&\left[(-\dot{v}_{,z})|_{z=\ell} r\sin\left(\Omega t + \frac{2\pi j}{N}\right) - (\dot{u}_{,z})|_{z=\ell} r\cos\left(\Omega t + \frac{2\pi j}{N}\right)\right] - (\dot{X}_n(t))_j\sin\beta\\ &\quad= \left[-\sum_{q=0}^{\infty}\dot{V}_q W_q'(\ell) r\sin\left(\Omega t + \frac{2\pi j}{N}\right) - \sum_{q=0}^{\infty}\dot{U}_q W_q'(\ell) r\cos\left(\Omega t + \frac{2\pi j}{N}\right)\right] - (\dot{X}_n(t))_j\sin\beta. \qquad (6)\end{aligned}$$

The dynamic terms such as displacement, velocity and acceleration associated with the transverse movement of the blade are written as

$$\eta(s,t) = \left[-\sum_{q=0}^{\infty} U_q(t)\sin\left(\frac{2\pi j}{N}\right) + \sum_{q=0}^{\infty} V_q(t)\cos\left(\frac{2\pi j}{N}\right)\right] W_q(\ell)\cos\beta + \sum_{n=1}^{\infty}(X_n(t))_j(Y_n(s))_j, \qquad (7)$$

$$\dot{\eta}(s,t) = \left[-\sum_{q=0}^{\infty} \dot{U}_q(t)\sin\left(\frac{2\pi j}{N}\right) + \sum_{q=0}^{\infty} \dot{V}_q(t)\cos\left(\frac{2\pi j}{N}\right)\right] W_q(\ell)\cos\beta + \sum_{n=1}^{\infty}(\dot{X}_n(t))_j(Y_n(s))_j, \qquad (8)$$

$$\ddot{\eta}(s,t) = \left[-\sum_{q=0}^{\infty} \ddot{U}_q(t)\sin\left(\frac{2\pi j}{N}\right) + \sum_{q=0}^{\infty} \ddot{V}_q(t)\cos\left(\frac{2\pi j}{N}\right)\right] W_q(\ell)\cos\beta + \sum_{n=1}^{\infty}(\ddot{X}_n(t))_j(Y_n(s))_j. \qquad (9)$$

The assumed trial function for the lateral deflection $\eta(s,t)$ in Eq. (4) is substituted in the beam–column bending equation of motion (1). After defining a set of mode shapes or the displacement

functions as $Y_n(s)$, which satisfies the geometric boundary conditions, we use the Galerkin's method to convert the governing partial differential equation (1) into a set of ordinary differential equations in terms of time-dependent variables such as $X_n(t)$, $U_q(t)$, $V_q(t)$, etc. The external forces in the equation of motion for the blade is caused by the friction force at the blade tip, which is trying to deform the cantilever blade in the direction opposite to the direction of motion, and its magnitude is $\mu F_a \cos\beta$. As described earlier, the axial force F_a being a contact-compressive load in the equation, its non-zero value will always be negative. Thus, the pth mode shape component of the external force vector on the right-hand side of the equation can be written as $\mu F_a \cos\beta\, Y_p(L)$.

Due to shaft bending and disk rotation, the rotary inertia and gyroscopic effects introduce additional velocity-dependent terms such as $\dot{X}_q(t)$, $\dot{U}_m(t)$, $\dot{V}_m(t)$ in the equation. Thus, in the matrix form using the standard summation convention of repeated indices such as '$_m$' and '$_q$', the pth equation of motion for a typical jth blade is written as

$$[M_{pm}]_{xj}\sum_{m=0}^{\infty}\ddot{U}_m + [M_{pm}]_{yj}\sum_{m=0}^{\infty}\ddot{V}_m + [C_{pm}]_{xj}\sum_{m=0}^{\infty}\dot{U}_m + [C_{pm}]_{yj}\sum_{m=0}^{\infty}\dot{V}_m + [M_{pq}](\ddot{X}_q)_j + [C_{pq}](\dot{X}_q)_j + [K_{pm}]_{xj}\sum_{m=0}^{\infty}U_m + [K_{pm}]_{yj}\sum_{m=0}^{\infty}V_m + [K_{pq}](X_q)_j = \mu(F_a)_j\cos\beta\, Y_p(L) \tag{10}$$

and the additional terms for the support motion are

$$[K_{p0}]_{xj}U_0 + [K_{p0}]_{yj}V_0 + [C_{p0}]_{xj}\dot{U}_0 + [C_{p0}]_{yj}\dot{V}_0 + [M_{p0}]_{xj}\ddot{U}_0 + [M_{p0}]_{yj}\ddot{V}_0, \tag{11}$$

where

$$[K_{p0}]_{xj} = [-(EI)_b Y_p'''(0) - \pi^2\Omega^2(\rho A)_b[(R+r)/2]]\sin\left(\frac{2\pi j}{N} - \beta\right),$$

$$[K_{p0}]_{yj} = [-(EI)_b Y_p'''(0) + \pi^2\Omega^2(\rho A)_b[(R+r)/2]]\cos\left(\frac{2\pi j}{N} - \beta\right),$$

$$[M_{p0}]_{xj} = -\left[(\rho A)_b\sin\left(\frac{2\pi j}{N}\right)\cos\beta\int_0^L Y_p\,\mathrm{d}s\right] = -(\rho AL)_b\sin\left(\frac{2\pi j}{N}\right)\cos\beta = -M_b\sin\left(\frac{2\pi j}{N}\right)\cos\beta,$$

$$[C_{p0}]_{xj} = -C_t\sin\left(\frac{2\pi j}{N}\right)\cos\beta\int_0^L Y_p\delta(s-L)\,\mathrm{d}s = -C_t\sin\left(\frac{2\pi j}{N}\right)\cos\beta\, Y_p(L),$$

$$[M_{p0}]_{yj} = \left[(\rho A)_b\cos\left(\frac{2\pi j}{N}\right)\cos\beta\int_0^L Y_p\,\mathrm{d}s\right] = (\rho AL)_b\cos\left(\frac{2\pi j}{N}\right)\cos\beta = M_b\cos\left(\frac{2\pi j}{N}\right)\cos\beta,$$

$$[C_{p0}]_{yj} = C_t\cos\left(\frac{2\pi j}{N}\right)\cos\beta\int_0^L Y_p\delta(s-L)\,\mathrm{d}s = C_t\cos\left(\frac{2\pi j}{N}\right)\cos\beta\, Y_p(L).$$

In the global frame of reference, the complete equation of motion of any typical jth blade of the blade-cascade mounted on a flexible rotor–disk system reduces to

$$
\begin{aligned}
&- M_b \sin\left(\frac{2\pi j}{N}\right)\ddot{U}_0 \\
&+ \left[-\left[\sum_{i=1}^{N_b}(D^b_{xx})_i + C_t\right]\cos\beta\sin\left(\frac{2\pi j}{N}\right) + \left[\sum_{i=1}^{N_b}(D^b_{yx})_i\right]\cos\beta\cos\left(\frac{2\pi j}{N}\right)\right]\dot{U}_0 \\
&+ \begin{bmatrix} -(EI)_b Y'''_m(0)\sin\left(\frac{2\pi j}{N}-\beta\right) - \pi^2\Omega^2(\rho A)_b \sin\left(\frac{2\pi j}{N}-\beta\right)[(R+r)/2] \\ -\left[\sum_{i=1}^{N_b}(S^b_{xx})_i + K_{rub}\right]\cos\beta\sin\left(\frac{2\pi j}{N}\right) + \left[\sum_{i=1}^{N_b}(S^b_{yx})_i - \mu K_{rub}\right]\cos\beta\cos\left(\frac{2\pi j}{N}\right) \end{bmatrix} U_0 \\
&+ M_b\cos\left(\frac{2\pi j}{N}\right)\ddot{V}_0 \\
&+ \left[-\left[\sum_{i=1}^{N_b}(D^b_{xy})_i\right]\cos\beta\sin\left(\frac{2\pi j}{N}\right) + \left[\sum_{i=1}^{N_b}(D^b_{yy})_i + C_t\right]\cos\beta\cos\left(\frac{2\pi j}{N}\right)\right]\dot{V}_0 \\
&+ \begin{bmatrix} -(EI)_b Y'''_m(0)\cos\left(\frac{2\pi j}{N}-\beta\right) + \pi^2\Omega^2(\rho A)_b \cos\left(\frac{2\pi j}{N}-\beta\right)[(R+r)/2] \\ -\left[\sum_{i=1}^{N_b}(S^b_{xy})_i + \mu K_{rub}\right]\cos\beta\sin\left(\frac{2\pi j}{N}\right) + \left[\sum_{i=1}^{N_b}(S^b_{yy})_i + K_{rub}\right]\cos\beta\cos\left(\frac{2\pi j}{N}\right) \end{bmatrix} V_0 \\
&- (\rho A)_b \sin\left(\frac{2\pi j}{N}\right)\left[\sum_{q=1} W_q(\ell)\int_0^L Y_m(s)\,\mathrm{d}s + W'_q(\ell)\cos^2\left(\frac{2\pi j}{N}\right)\int_0^L Y'_m(s)(s+r)^2\,\mathrm{d}s\right]\ddot{U}_q \\
&- C_t \sin\left(\frac{2\pi j}{N}\right)\cos\beta\, W_q(\ell)\int_0^L Y_m\delta(s-L)\,\mathrm{d}s\sum_{q=1}\dot{U}_q \\
&- \Omega(\rho A)_b \sin\beta\cos\left(\frac{2\pi j}{N}\right)\int_0^L Y'_m(s)(s+r)^2\,\mathrm{d}s\sum_{q=1} W'_q(\ell)\dot{U}_q \\
&+ \sum_{q=1}\begin{bmatrix} -(EI)_s W'''_q(\ell) - \pi^2\Omega^2(\rho A)_b W_q(\ell)[(R+r)/2] \\ -(EI)_b Y'''_m(0) W_q(\ell) + (EI)_b Y''_m(0) W'_q(\ell) \end{bmatrix}\sin\left(\frac{2\pi j}{N}-\beta\right) U_q \\
&+ (\rho A)_b \cos\left(\frac{2\pi j}{N}\right)\left[\sum_{q=1} W_q(\ell)\int_0^L Y_m(s)\,\mathrm{d}s + W'_q(\ell)\sin^2\left(\frac{2\pi j}{N}\right)\int_0^L Y'_m(s)(s+r)^2\,\mathrm{d}s\right]\ddot{V}_q \\
&+ C_t\cos\left(\frac{2\pi j}{N}\right)\cos\beta\, W_q(\ell)\int_0^L Y_m\delta(s-L)\,\mathrm{d}s\sum_{q=1}\dot{V}_q \\
&- \Omega(\rho A)_b \sin\beta\sin\left(\frac{2\pi j}{N}\right)\int_0^L Y'_m(s)(s+r)^2\,\mathrm{d}s\sum_{q=1} W'_q(\ell)\dot{V}_q
\end{aligned}
$$

$$
\begin{aligned}
&+ \sum_{q=1}\begin{bmatrix} -(EI)_s W_q'''(\ell) + \pi^2\Omega^2(\rho A)_b W_q(\ell)[(R+r)/2] \\ -(EI)_b Y_m'''(0) W_q(\ell) + (EI)_b Y_m''(0) W_q'(\ell) \end{bmatrix} \cos\left(\frac{2\pi j}{N} - \beta\right) V_q \\
&+ (\rho A)_b \left[\sum_{n=1}^{\infty} \int_0^L Y_m Y_n \,\mathrm{d}s\right] (\ddot{X}_n)_j + C_t \left[\sum_{n=1}^{\infty} \int_0^L Y_m Y_n \delta(s-L)\,\mathrm{d}s\right] (\dot{X}_n)_j \\
&+ \sum_{n=1}\begin{bmatrix} (EI)_b \int_0^L Y_m\, Y_n'''' \,\mathrm{d}s + (\rho A)_b \Omega^2 \int_0^L (s+r) Y_m Y_n' \,\mathrm{d}s \\ -\dfrac{(\rho A)_b \Omega^2}{2} \int_0^L (2rL + L^2 - 2rs - s^2) Y_m Y_n'' \,\mathrm{d}s - F_a \int_0^L Y_m Y_n'' \,\mathrm{d}s \end{bmatrix} (X_n)_j \\
&= -\mu |F_a| \cos\beta\, Y_m(L). \qquad (12)
\end{aligned}
$$

In the above equation, all the terms related to the shaft such as $(EI)_s$ and W_q, U_q, V_q, etc. and bearing damping and stiffness terms such as $[D^b_{xx}]_i$, $[D^b_{xy}]_i$, $[D^b_{yx}]_i$, $[D^b_{yy}]_i$, $[S^b_{xx}]_i$, $[S^b_{xy}]_i$, $[S^b_{yx}]_i$, and $[S^b_{yy}]_i$, etc. will be explained in a later section. Here, the lateral deformation of the blade is assumed in the form of a shape function $Y_n(s)$ such that it satisfies all the forced boundary conditions naturally, which is

$$Y_n(s) = a_{1n}s^3 + a_{2n}s^2 + a_{3n}s + \sin(\beta_n s), \qquad (13)$$

where $\beta_n = (2n-1)\pi/(2L)$. Thus,

$$Y_n'(s) = 3a_{1n}s^2 + 2a_{2n}s + a_{3n} + \beta_n \cos(\beta_n s),$$

$$Y_n''(s) = 6a_{1n}s + 2a_{2n} - (\beta_n)^2 \sin(\beta_n s),$$

$$Y_n'''(s) = 6a_{1n} - (\beta_n)^3 \cos(\beta_n s), \quad Y_n''''(s) = (\beta_n)^4 \sin(\beta_n s).$$

On applying the forced and natural boundary conditions as $Y_n(0) = 0$, $Y_n'(0) = 0$, and $EIY_n''(L) = 0$, $EIY_n'''(L) - F_a Y_n'(L) = 0$, we get

$$a_{1n} = \frac{\beta_n F_a [L\beta_n \sin(\beta_n L) - 1]}{6(EI)_{blade} + 3F_a L^2},$$

$$a_{2n} = -3a_{1n}L + \frac{(\beta_n)^2}{2}\sin(\beta_n L) = \frac{(\beta_n)^2}{2}\sin(\beta_n L) - \frac{\beta_n F_a [L\beta_n \sin(\beta_n L) - 1]L}{2(EI)_{blade} + F_a L^2},$$

$$a_{3n} = -\beta_n.$$

One can choose a displacement function to satisfy only the geometric boundary conditions in which case the coefficients are simplified as

$$a_{1n} = 0, \quad a_{2n} = \frac{(\beta_n)^2}{2}\sin(\beta_n L), \quad a_{3n} = -\beta_n.$$

Thus, the global components of the blade axial forces acting in the radial direction of the rotor shaft become either a function of θ for acceleration or for a constant angular velocity Ω,

$$(F_x)_j = (F_a)_j \cos\left(\frac{2\pi j}{N} + \theta\right) = (F_a)_j \cos\left(\frac{2\pi j}{N} + \Omega t\right), \tag{14}$$

$$(F_y)_j = (F_a)_j \sin\left(\frac{2\pi j}{N} + \theta\right) = (F_a)_j \sin\left(\frac{2\pi j}{N} + \Omega t\right). \tag{15}$$

3. Rotordynamic equations for shaft with rub

In this section, we will develop the governing dynamical equation for the rotor shaft in all its complexities. The current approach of starting with the Euler–Bernoulli's beam differential equation is very similar to one used by several previous authors [23,24]. This method was extended [25] for studying the whirl speeds and vibration modes of a flexible rotating shaft with gyroscopic effect and simply-supported end-conditions. Using an identical formulation, the impact response of an elastically-supported rotating disk–spindle system has been solved by Parker [26]. Lee and Zei [27,28] have addressed the problem of continuous flexible shaft with bearing supports at discrete locations in a closed form. For stability analysis of a flexible shaft, Khader [29] used the energy method to derive the equations of motion of a cantilever disk–rotor system. In a recent paper, Zheng and Hasebe [30] tried to determine the chaotic response and long-term transient dynamic behavior of multi-degrees-of-freedom rotor-bearing system in the time-domain.

For the governing dynamical equation of the rotor shaft, which in general, is a long hollow circular cylinder, we will focus on an overhung disk–rotor bladed system (see Fig. 3). The shaft (inside radius $= r_i$ and the outside radius $= r_o$) is spinning inside a bearing at one end ($z = z_1 = 0$), and is supported at intermediate discrete axial locations ($z = z_i$). As a general case, these support bearing may not necessarily be symmetrical in the x–y plane and as such for any typical ith bearing located at $z = z_i$, their dynamic stiffness $[\boldsymbol{S}]_b$ and damping $[\boldsymbol{D}]_b$ in matrix form are written as

$$[\boldsymbol{S}]_b = \begin{bmatrix} S^b_{xx} & S^b_{xy} & & \\ S^b_{yx} & S^b_{yy} & & \\ & & B^b_{xx} & \\ & & & B^b_{yy} \end{bmatrix}_i, \quad [\boldsymbol{D}]_b = \begin{bmatrix} D^b_{xx} & D^b_{xy} \\ D^b_{yx} & D^b_{yy} \end{bmatrix}_i. \tag{16}$$

Here, $[S^b_{xx}]_i$, $[S^b_{xy}]_i$, $[S^b_{yx}]_i$, and $[S^b_{yy}]_i$ have the dimensions of linear stiffness as force per unit length, and $[B^b_{xx}]_i$, $[B^b_{xx}]_i$ have the dimensions of bending stiffness as moment/unit radian. For short bearings with no axial restraints, the $[B^b_{xx}]_i$ and $[B^b_{yy}]_i$ will be zero, but for long-bearings with axial load carrying capability the terms $[B^b_{xx}]_i$ and $[B^b_{yy}]_i$ are non-zero. The reaction force at the bearing support locations due to stiffness terms can be written as

$$(F_x)_b = [-S^b_{xx}u(z_i,t) - B^b_{xx}u_{,zz}(z_i,t) - S^b_{xy}v(z_i,t)] \quad \text{at } z = z_i, \tag{17}$$

$$(F_y)_b = [-S^b_{yx}u(z_i,t) - B^b_{yx}v_{,zz}(z_i,t) - S^b_{yy}v(z_i,t)] \quad \text{at } z = z_i. \tag{18}$$

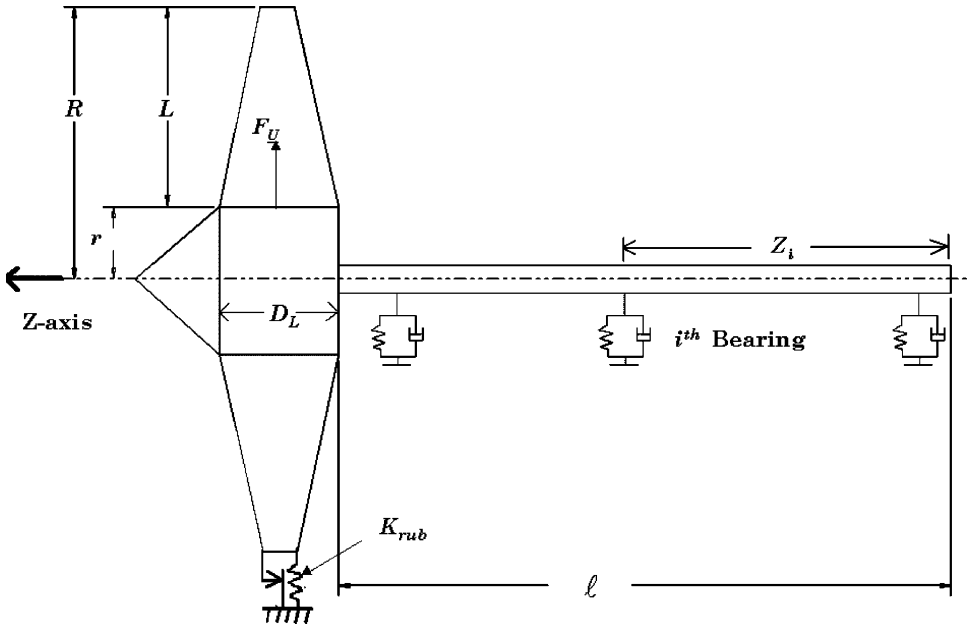

Fig. 3. Fan rotor shaft supported on multiple bearings: number of blades = N, mass density = $(\rho)_s$, cross-sectional area = $(A)_s = \pi(r_o^2 - r_i^2)$, flexural rigidity = $(EI)_s$, Coulomb friction force: $F_x = \mu K_{rub} v(\ell, t)$, $F_y = -\mu K_{rub} u(\ell, t)$. For the ith bearing, stiffness = $[\boldsymbol{S}]i$; and damping = $[\boldsymbol{D}]i$. In case of air gap between the blade tip and the outer case, $K_{rub} = 0$.

It should be pointed out that we are carrying the damping terms $[D^b_{xx}]_i$, $[D^b_{xy}]_i$, $[D^b_{yx}]_i$, and $[D^b_{yy}]_i$ in the bearing equations to keep the mathematical derivations general enough for all types of bearings. However, in jet engines the rotor is supported on ball and roller bearings, which have practically no damping as opposed to the journal bearings in which oil film provide significant amount of damping for the lateral motion of the shaft. In Eqs. (17) and (18), $u(z_i, t)$ and $v(z_i, t)$ are the deflections of the shaft at the bearing support locations. We assume that the fan disk with all the blades can be considered as a lumped mass 'M' located at $z = \ell$ and having a diametral mass moment of inertia as J. At this point, we introduce the notations for the shaft mass density as '$(\rho)_s$', Young's modulus as '$(E)_s$', cross-sectional area '$(A)_s$' and its cross-sectional area moment of inertia as '$(I)_s$', and the critical viscous damping coefficient of the shaft 'H' as

$$H = \frac{\ell^2}{\pi^2}[EI\rho A]_s^{1/2}. \tag{19}$$

The governing equations of motion in the stationary global frame of reference of x and y directions, defined as $u(z, t)$ and $v(z, t)$ respectively, for the fan rotor spinning at the angular velocity of Ω radians per second during the blade tip rub are

$$\left[(EI)_s + 2\zeta H\frac{\partial}{\partial t}\right]u_{,zzzz} + (\rho A)_s u_{,tt} - I_d u_{,zztt} - 2I_d\Omega v_{,zzt} + 2\zeta H\Omega v_{,zzzz} + T(t)v_{,zzz}$$
$$- P(t)u_{,zz} + \sum_{i=1}^{N_b}[S^b_{xx}u + S^b_{xy}v + B^b_{xx}u_{,zz} + D^b_{xx}u_{,t} + D^b_{xy}v_{,t}]\delta(z - zi)$$

$$+ [Mu_{,tt} - Ju_{,zztt} - 2J\Omega v_{,zzt}]\delta(z-\ell)$$
$$+ K_{rub}[(u - R(u,z)^2) + \mu(v - R(v,z)^2)]\delta(z-\ell) = q_x(z,t), \tag{20}$$

$$\left[(EI)_s + 2\zeta H\frac{\partial}{\partial t}\right]v_{,zzzz} + (\rho A)_s v_{,tt} - I_d v_{,zztt} + 2I_d\Omega u_{,zzt} - 2\zeta H\Omega u_{,zzzz} - T(t)u_{,zzz}$$
$$- P(t)v_{,zz} + \sum_{i=1}^{N_b}[S^b_{yx}u + S^b_{yy}v + B^b_{yy}v_{,zz} + D^b_{yx}u_{,t} + D^b_{yy}v_{,t}]\delta(z-z_i)$$
$$+ [Mv_{,tt} - Jv_{,zztt} + 2J\Omega u_{,zzt}]\delta(z-\ell)$$
$$+ K_{rub}[(v - R(v,z)^2) - \mu(u - R(u,z)^2)]\delta(z-\ell) = q_y(z,t). \tag{21}$$

The presence of skew-symmetric stiffness terms due to Coulomb friction in Eqs. (20) and (21) highlights the destabilizing effect of the rub. In order to determine whether a particular rub is actually destabilizing to the rotor or, if it can ride-through the rub action requires that the blade tip movement be computed very precisely, which forces us to include the non-linear terms in the blade-tip movement calculation. Due to bending of the shaft and the resulting rotation of the disk and blades, the term containing the Coulomb friction effect at the blade tip, namely, $R(u_{,z})^2$ and $R(v_{,z})^2$ are truly non-linear, and are included for an accurate determination of the rub condition. However under small rotation assumption, they can be reduced into linear terms with a rotation factor 'e' as

$$R(u_{,z})^2 \approx eRu_{,z}, \quad R(v_{,z})^2 \approx eRv_{,z}.$$

Depending upon the fan blade tip radius 'R' the typical value of the rotation factor 'e' will vary anywhere from 0.01 to 0.1. In the linearization process under small rotation assumptions, for the direct rub stiffness terms, we can write

$$(u_{,z})^2 \approx 0, \quad (v_{,z})^2 \approx 0.$$

4. Mathematical derivations of external loads for different rub conditions

The most common external load in any rotordynamic problem is the rotating load vector due to unbalance. During the normal operation of an aero-engine fan at a given speed, the gas loads F_G on the blades apply a steady state load torque on the shaft. For any other speed this load torque is proportional to the square of the speed. If the fan blade tip rub takes place under these conditions, then both the torque due to F_G and Coulomb friction are opposite to the direction of rotation. However, during the wind-milling operation the gas load F_G becomes the driving torque and the Coulomb friction like always is acting opposite to the direction of motion trying to straighten the blades.

The blade tip-rub introduces additional loads making the loading on the shaft much more complex than a simple rotating unbalance. In the rotordynamic equations (20) and (21), all the loads transferred to the shaft through the blades can be treated like external loads. When the tip of the blades start rubbing against the inner surface of the containment structure, then depending upon the magnitude of the radial load along the blade stacking axis (F_a), the blade tips can either

skate on the inner surface if it is sufficiently hard or, they can cut through the inner surface if it is relatively soft. If ultimate shear strength of the inner surface is τ, and the radial incursion of the blade tip or the interference with the inner surface is 'ε' then for a blade of the chord length 'c' at the tip, the condition for either skating or cutting-through can be established as follows: skating will occur if $\boldsymbol{F}_a < 2\tau\varepsilon c$, and cutting-through will occur if $\boldsymbol{F}_a > 2\tau\varepsilon c$.

If the inner surface material has been cut-through, then as the tip-rub progresses, the cut material will be pushed away from the path of the rotating blade tip like by ploughing action. As such, the blade tip rub produces the following loads on the rotor shaft.

(1) During skating of the blade tip on the inner surface with coefficient of friction 'μ 'and the blade tip stagger angle 'β', the radial shear load on the shaft by a typical jth blade, the bending load in the normal direction on a typical jth blade, and the torque on the shaft by a typical jth blade are given, respectively, by

$$(F_a)_j, \quad \mu(F_a)_j \cos\beta, \quad \mu(F_a)_j(r+L). \tag{22}$$

(2) During ploughing action of the blade tip of the inner surface of the filler material with density '$(\rho)_c$' and blade tip tangential velocity 'ΩR', the radial shear load on the shaft by a typical jth blade, the radial incursion 'ε', and the bending load in the normal direction on a typical jth blade are given by

$$(F_a)_j, \quad (F_a)_j/2\tau c, \quad \mu(F_a)_j \cos\beta,$$

Furthermore, the torque on the shaft by a typical jth blade is

$$\tfrac{1}{2}(\rho)_c(\Omega R\cos\beta)^2 \varepsilon c\cos\beta(r+L) = \tfrac{1}{2}(\rho)_c(\Omega R\cos\beta)^2((F_a)_j/2\tau)\cos\beta(r+L),$$

and the axial load on the shaft by a typical jth blade is

$$\tfrac{1}{2}(\rho)_c(\Omega R\cos\beta)^2 \varepsilon c\sin\beta = \tfrac{1}{2}(\rho)_c(\Omega R\cos\beta)^2((F_a)_j/2\tau)\sin\beta. \tag{23}$$

Also, in the above equation, $(F_a)_j$ is a function of time 't'. Thus, the shaft sees only steady axial pull due to the gas load on the blades F_G, however, it has both steady state and time-varying torque terms in the left-hand side of Eqs. (20) and (21):

$$P(t) = P_0 + P_t = NF_G \sin\beta, \tag{24}$$

$$T(t) = T_0 + T_t = NF_G(r+0.5L)\cos\beta + \sum_{j=1}^{N} \mu(F_a)_j(r+L). \tag{25}$$

In a rigorous sense, the above relationship for $P(t)$ and $T(t)$ shown in Eqs. (24) and (25) are correct only for a constant speed. During acceleration and deceleration of the rotor, Ω is no longer constant and F_G as well as $(F_a)_j$ are also time-dependent, which make the entire dynamic even highly non-linear. The additional load during the plowing action of the blade-tip against the relatively soft filler material in the case imparts a pulse load on the shaft and should be treated accordingly in the dynamical equation for the shaft.

5. Application of Galerkin's method to the shaft equations of motion

The solution of Eqs. (20) and (21) may be assumed in the following form of time 't' and spatial variable 'z':

$$u(z,t)=\sum_{m=0}^{\infty} U_m(t)W_m(z)=U_0(t)+\sum_{m=1}^{\infty} U_m(t)[1-\cos\alpha_m z], \tag{26}$$

$$v(z,t)=\sum_{m=0}^{\infty} V_m(t)W_m(z)=V_0(t)+\sum_{m=1}^{\infty} V_m(t)[1-\cos\alpha_m z], \tag{27}$$

where $\alpha_m=(2m-1)\pi/(2\ell)$. Thus,

$$W_0(z)=1,\quad W_m(z)=1-\cos(\alpha_m z),\quad W'_m(z)=\alpha_m\sin(\alpha_m z),$$

$$W''_m(z)=(\alpha_m)^2\cos(\alpha_m z),\quad W'''_m(z)=-(\alpha_m)^3\sin(\alpha_m z),\quad W''''_m(z)=-(\alpha_m)^4\cos(\alpha_m z).$$

Applying the Galerkin's method, one obtains a set of ordinary differential equations of which a typical kth equation is

$$\int_0^{\ell}\Re(\boldsymbol{u},\boldsymbol{v})\boldsymbol{W_k}(\boldsymbol{z})\,\mathrm{d}\boldsymbol{z}=\boldsymbol{0}. \tag{28}$$

Since the natural boundary condition of shear force equal to zero at the disk end is not satisfied for $z=\ell$, the nth algebraic equation for the set of simultaneous equations is written as

$$\begin{aligned}
&\sum_{m=0}^{\infty}\begin{bmatrix}
(EI)_s U_m\int_0^{\ell} W''''_m W_n\,\mathrm{d}z+2\zeta H\dot{U}_m\int_0^{\ell} W''''_m W_n\,\mathrm{d}z+(\rho A)_s\ddot{U}_m\int_0^{\ell} W_m W_n\,\mathrm{d}z-I_d\ddot{U}_m\int_0^{\ell} W''_m W_n\,\mathrm{d}z\\
-2I_d\Omega\dot{V}_m\int_0^{\ell} W''_m W_n\,\mathrm{d}z+2\zeta H\Omega V_m\int_0^{\ell} W''''_m W_n\,\mathrm{d}z+T(t)V_m\int_0^{\ell} W'''_m W_n\,\mathrm{d}z-P(t)U_m\int_0^{\ell} W''_m W_n\,\mathrm{d}z\\
+\sum_{i=1}^{N_b}[S^b_{xx}U_m+S^b_{xy}V_m+D^b_{xx}\dot{U}_m+D^b_{xy}\dot{V}_m]\int_0^{\ell} W_m W_n\delta(z-z_i)\,\mathrm{d}z+\sum_{i=1}^{N_b}[B^b_{xx}U_m]\int_0^{\ell} W''_m W_n\delta(z-z_i)\,\mathrm{d}z
\end{bmatrix}\\
&+[M\ddot{U}_m W_m(\ell)W_n(\ell)+J\ddot{U}_m W'_m(\ell)W'_n(\ell)+2J\Omega\dot{V}_m W'_m(\ell)W'_n(\ell)]\\
&+K_{rub}[U_m W_m(\ell)W_n(\ell)+\mu(V_m W_m(\ell)W_n(\ell)-eRV_m W'_m(\ell)W_n(\ell))]\\
&+P(t)U_m W'_m(\ell)W_n(\ell)-T(t)V_m W'_m(\ell)W'_n(\ell)\\
&-F_U\cos(\theta+\phi)\delta(z-\ell)W_n(\ell)-(EI)_s U_m W'''_m(\ell)W_n(\ell)+(EI)_s U_m W''_m(\ell)W'_n(\ell)\\
&=\int_0^{\ell} R_x(z)W_n\,\mathrm{d}z=0.
\end{aligned} \tag{29}$$

$$\sum_{m=0}^{\infty}\begin{bmatrix}(EI)_s V_m\int_0^\ell W_m''''W_n\,\mathrm{d}z+2\zeta H\dot V_m\int_0^\ell W_m''''W_n\,\mathrm{d}z+(\rho A)_s\ddot V_m\int_0^\ell W_mW_n\,\mathrm{d}z-I_d\ddot V_m\int_0^\ell W_m''W_n\,\mathrm{d}z\\ +2I_d\Omega\dot U_m\int_0^\ell W_m''W_n\,\mathrm{d}z-2\zeta H\Omega U_m\int_0^\ell W_m''''W_n\,\mathrm{d}z-T(t)U_m\int_0^\ell W_m''''W_n\,\mathrm{d}z-P(t)V_m\int_0^\ell W_m''W_n\,\mathrm{d}z\\ +\sum_{i=1}^{N_b}[S^b_{xy}U_m+S^b_{yy}V_m+D^b_{xy}\dot U_m+D^b_{yy}\dot V_m]\int_0^\ell W_mW_n\delta(z-z_i)\,\mathrm{d}z+\sum_{i=1}^{N_b}[B^b_{yy}V_m]\int_0^\ell W_m''W_n\delta(z-z_i)\,\mathrm{d}z\end{bmatrix}$$
$$+\ [M\ddot V_mW_m(\ell)W_n(\ell)+J\ddot V_mW_m'(\ell)W_n'(\ell)-2J\Omega\dot U_mW_m'(\ell)W_n'(\ell)]$$
$$+\ K_{rub}[V_mW_m(\ell)W_n(\ell)-\mu(U_mW_m(\ell)W_n(\ell)-eRU_mW_m'(\ell)W_n(\ell))]$$
$$+\ P(t)V_mW_m'(\ell)W_n(\ell)+T(t)U_mW_m'(\ell)W_n'(\ell)$$
$$-F_U\sin(\theta+\phi)\delta(z-\ell)W_n(\ell)-(EI)_sV_mW_m'''(\ell)W_n(\ell)+(EI)_sV_mW_m''(\ell)W_n'(\ell)$$
$$=\int_0^\ell R_y(z)W_n\,\mathrm{d}z=0. \tag{30}$$

The Galerkin's method simplifies partial differential equations (29) and (30) into a set of coupled second-order differential equations in terms of time-dependent variables. For determining the $U_0(t)$ and $V_0(t)$ terms in the assumed displacement functions. The rigid body equation is obtained by setting $n=0$, and using $W_0(z)=1$ in the above set of equations, yields

$$\sum_{m=0}^{\infty}\begin{bmatrix}(EI)_sU_m\int_0^\ell W_m''''\,\mathrm{d}z+2\zeta H\dot U_m\int_0^\ell W_m''''\,\mathrm{d}z+(\rho A)_s\ddot U_m\int_0^\ell W_m\,\mathrm{d}z-I_d\ddot U_m\int_0^\ell W_m''\,\mathrm{d}z\\ -2I_d\Omega\dot V_m\int_0^\ell W_m''\,\mathrm{d}z+2\zeta H\Omega V_m\int_0^\ell W_m''''\,\mathrm{d}z+T(t)V_m\int_0^\ell W_m'''\,\mathrm{d}z-P(t)U_m\int_0^\ell W_m''\,\mathrm{d}z\\ +\sum_{i=1}^{N_b}[S^b_{xx}U_m+S^b_{xy}V_m+D^b_{xx}\dot U_m+D^b_{xy}\dot V_m]\int_0^\ell W_m\delta(z-z_i)\,\mathrm{d}z+\sum_{i=1}^{N_b}[B^b_{xx}U_m]\int_0^\ell W_m''\delta(z-z_i)\,\mathrm{d}z\end{bmatrix}$$
$$+\ M\ddot U_mW_m(\ell)+K_{rub}[U_mW_m(\ell)+\mu(V_mW_m(\ell)-eRV_mW_m'(\ell))]$$
$$-\ F_U\cos(\theta+\phi)-(EI)_sU_m[W_m'''(\ell)]+P(t)U_m[W_m'(\ell)]=0, \tag{31}$$

$$\sum_{m=0}^{\infty}\begin{bmatrix}(EI)_sV_m\int_0^\ell W_m''''\,\mathrm{d}z+2\zeta H\dot V_m\int_0^\ell W_m''''\,\mathrm{d}z+(\rho A)_s\ddot V_m\int_0^\ell W_m\,\mathrm{d}z-I_d\ddot V_m\int_0^\ell W_m''\,\mathrm{d}z\\ +2I_d\Omega\dot U_m\int_0^\ell W_m''\,\mathrm{d}z-2\zeta H\Omega U_m\int_0^\ell W_m''''\,\mathrm{d}z-T(t)U_m\int_0^\ell W_m'''\,\mathrm{d}z-P(t)V_m\int_0^\ell W_m''\,\mathrm{d}z\\ +\sum_{i=1}^{N_b}[S^b_{xy}U_m+S^b_{yy}V_m+D^b_{xy}\dot U_m+D^b_{yy}\dot V_m]\int_0^\ell W_m\delta(z-z_i)\,\mathrm{d}z+\sum_{i=1}^{N_b}[B^b_{yy}V_m]\int_0^\ell W_m''\delta(z-z_i)\,\mathrm{d}z\end{bmatrix}$$
$$+\ M\ddot V_mW_m(\ell)+K_{rub}[V_mW_m(\ell)-\mu(U_mW_m(\ell)-eRU_mW_m'(\ell))]$$
$$-\ F_U\sin(\theta+\phi)-(EI)_sV_m[W_m'''(\ell)]+P(t)V_m[W_m'(\ell)]=0. \tag{32}$$

On expanding the generalized co-ordinates such as U_m and V_m we get

$$\left[(\rho A)_s\int_0^\ell W_n\,\mathrm{d}z+M\right]\ddot U_0+\left[\sum_{i=1}^{N_b}(D^b_{xx})_iW_n(z_i)\right]\dot U_0$$
$$+\left[\sum_{i=1}^{N_b}[(S^b_{xx})_iW_n(z_i)+(B^b_{xx})_iW_n''(z_i)]+K_{rub}W_n(\ell)+P(t)W_n'(\ell)\right]U_0$$
$$+\left[\sum_{i=1}^{N_b}(D^b_{xy})_iW_n(z_i)\right]\dot V_0+\left[\sum_{i=1}^{N_b}(S^b_{xy})_iW_n(z_i)+\mu K_{rub}W_n(\ell)\right]V_0$$
$$+\sum_{m=1}^{\infty}\left[(\rho A)_s\int_0^\ell W_mW_n\,\mathrm{d}z-I_d\int_0^\ell W_m''W_n\,\mathrm{d}z+JW_m'(\ell)W_n'(\ell)+MW_m(\ell)W_n(\ell)\right]\ddot U_m$$

$$
\begin{aligned}
&+\sum_{m=1}^{\infty}\left[2\zeta H\int_0^{\ell} W_m''''W_n\,\mathrm{d}z+\sum_{i=1}^{N_b}(D_{xx}^b)_i W_m(z_i)W_n(z_i)\right]\dot{U}_m\\
&+\sum_{m=1}^{\infty}\left[\begin{array}{c}(EI)_s\int_0^{\ell} W_m''''W_n\,\mathrm{d}z-(EI)_s W_m'''(\ell)W_n(\ell)\\ +\sum_{i=1}^{N_b}\left[(S_{xx}^b)_i W_m(z_i)W_n(z_i)+(B_{xx}^b)_i W_m''(z_i)W_n(z_i)\right]\\ -P(t)\int_0^{\ell} W_m''W_n\,\mathrm{d}z+P(t)W_m'(\ell)W_n(\ell)+K_{rub}W_m(\ell)W_n(\ell)\end{array}\right]U_m\\
&+\sum_{m=1}^{\infty}\left[\sum_{i=1}^{N_b}(D_{xy}^b)_i W_m(z_i)W_n(z_i)-2I_d\Omega\int_0^{\ell} W_m''W_n\,\mathrm{d}z+2J_D\Omega W_m'(\ell)W_n'(\ell)\right]\dot{V}_m\\
&+\sum_{m=1}^{\infty}\left[\begin{array}{c}\sum_{i=1}^{N_b}(S_{xy}^b)_i W_m(z_i)W_n(z_i)+T(t)\int_0^{\ell} W_m'''W_n\,\mathrm{d}z-T(t)W_m'(\ell)W_n'(\ell)\\ +\mu K_{rub}[W_m(\ell)W_n(\ell)-eRW_m'(\ell)W_n(\ell)]+2\zeta H\Omega\int_0^{\ell} W_m''''W_n\,\mathrm{d}z\end{array}\right]V_m\\
&-(\rho A)_b\sum_{j=1}^{N}\sin\left(\frac{2\pi j}{N}\right)\left[\sum_{q=1}W_n(\ell)\int_0^{L}Y_q(s)\,\mathrm{d}s+W_n'(\ell)\cos^2\left(\frac{2\pi j}{N}\right)\int_0^{L}Y_q'(s)(s+r)^2\,\mathrm{d}s\right](\ddot{X}_q)_j\\
&+\Omega W_n'(\ell)(\rho A)_b\sin\beta\sum_{j=1}^{N}\cos\left(\frac{2\pi j}{N}\right)\left[\sum_{q=1}\int_0^{L}Y_q'(s)(s+r)^2\,\mathrm{d}s\right](\dot{X}_q)_j\\
&-C_t\cos\beta W_n(\ell)\sum_{j=1}^{N}\sin\left(\frac{2\pi j}{N}\right)\left[\sum_{q=1}\int_0^{L}Y_q(s)\delta(s-L)\,\mathrm{d}s\right](\dot{X}_q)_j\\
&+\sum_{j=1}^{N}\left[\begin{array}{c}-(EI)_b Y_q'''(0)W_n(\ell)+(EI)_b Y_q''(0)W_n'(\ell)\\ -(EI)_s W_n'''(\ell)-\pi^2\Omega^2(\rho A)_b W_n(\ell)[(R+r)/2]\end{array}\right]\sin\left(\frac{2\pi j}{N}-\beta\right)(X_q)_j\\
&=\int_0^{\ell}F_U\left[W_n+W_n'\frac{D_L}{2}\right]\cos(\theta+\phi)\delta(z-\ell)\,\mathrm{d}z+\sum_{j=1}^{N}(F_a)_j\cos\left(\frac{2\pi j}{N}+\theta\right),
\end{aligned}
\tag{33}
$$

$$
\begin{aligned}
&\left[\sum_{i=1}^{N_b}(D_{yx}^b)_i W_n(z_i)\right]\dot{U}_0+\left[\sum_{i=1}^{N_b}(S_{yx}^b)_i W_n(z_i)-\mu K_{rub}W_n(\ell)\right]U_0\\
&\quad+\left[(\rho A)_s\int_0^{\ell}W_n\,\mathrm{d}z+M\right]\ddot{V}_0+\left[\sum_{i=1}^{N_b}(D_{yy}^b)_i W_n(z_i)\right]\dot{V}_0\\
&\quad+\left[\sum_{i=1}^{N_b}\left[(S_{yy}^b)_i W_n(z_i)+(B_{yy}^b)_i W_n''(z_i)\right]+K_{rub}W_n(\ell)+P(t)W_n'(\ell)\right]V_0\\
&\quad+\sum_{m=1}^{\infty}\left[\sum_{i=1}^{N_b}(D_{yx}^b)_i W_m(z_i)W_n(z_i)+2I_d\Omega\int_0^{\ell}W_m''W_n\,\mathrm{d}z-2J_D\Omega W_m'(\ell)W_n'(\ell)\right]\dot{U}_m\\
&\quad+\sum_{m=1}^{\infty}\left[\begin{array}{c}\sum_{i=1}^{N_b}(S_{yx}^b)_i W_m(z_i)W_n(z_i)-T(t)\int_0^{\ell}W_m'''W_n\,\mathrm{d}z+T(t)W_m'(\ell)W_n'(\ell)\\ -\mu K_{rub}[W_m(\ell)W_n(\ell)-eRW_m'(\ell)W_n(\ell)]-2\zeta H\Omega\int_0^{\ell}W_m''''W_n\,\mathrm{d}z\end{array}\right]U_m
\end{aligned}
$$

$$
\begin{aligned}
&+\sum_{m=1}^{\infty}\left[(\rho A)_s\int_0^{\ell} W_m W_n\,\mathrm{d}z - I_d\int_0^{\ell} W_m'' W_n\,\mathrm{d}z + JW_m'(\ell)W_n'(\ell) + MW_m(\ell)W_n(\ell)\right]\ddot{V}_m\\
&+\sum_{m=1}^{\infty}\left[2\zeta H\int_0^{\ell} W_m'''' W_n\,\mathrm{d}z + \sum_{i=1}^{N_b}(D_{yy}^b)_i W_m(z_i)W_n(z_i)\right]\dot{V}_m\\
&+\sum_{m=1}^{\infty}\left[\begin{array}{c}(EI)_s\int_0^{\ell} W_m'''' W_n\,\mathrm{d}z - (EI)_s W_m'''(\ell)W_n(\ell)\\ +\sum_{i=1}^{N_b}[(S_{yy}^b)_i W_m(z_i)W_n(z_i) + (B_{yy}^b)_i W_m''(z_i)W_n(z_i)]\\ -P(t)\int_0^{\ell} W_m'' W_n\,\mathrm{d}z + P(t)W_m'(\ell)W_n(\ell) + K_{rub}W_m(\ell)W_n(\ell)\end{array}\right]V_m\\
&+(\rho A)_b\sum_{j=1}^{N}\cos\left(\frac{2\pi j}{N}\right)\left[\sum_{q=1} W_n(\ell)\int_0^{L} Y_q(s)\,\mathrm{d}s + W_n'(\ell)\sin^2\left(\frac{2\pi j}{N}\right)\int_0^{L} Y_q'(s)(s+r)^2\,\mathrm{d}s\right](\ddot{X}_q)_j\\
&+\Omega W_n'(\ell)(\rho A)_b\sin\beta\sum_{j=1}^{N}\sin\left(\frac{2\pi j}{N}\right)\left[\sum_{q=1}\int_0^{L} Y_q'(s)(s+r)^2\,\mathrm{d}s\right](\dot{X}_q)_j\\
&+C_t\cos\beta W_n(\ell)\sum_{j=1}^{N}\cos\left(\frac{2\pi j}{N}\right)\left[\sum_{q=1}\int_0^{L} Y_q(s)\delta(s-L)\,\mathrm{d}s\right](\dot{X}_q)_j\\
&+\sum_{j=1}^{N}\left[\begin{array}{c}-(EI)_b Y_q'''(0)W_n(\ell) + (EI)_b Y_q''(0)W_n'(\ell)\\ -(EI)_s W_n'''(\ell) + \pi^2\Omega^2(\rho A)_b W_n(\ell)[(R+r)/2]\end{array}\right]\cos\left(\frac{2\pi j}{N}-\beta\right)(X_q)_j\\
&=\int_0^{\ell} F_U\left[W_n + W_n'\frac{D_L}{2}\right]\sin(\theta+\phi)\delta(z-\ell)\,\mathrm{d}z + \sum_{j=1}^{N}(F_a)_j\sin\left(\frac{2\pi j}{N}+\theta\right). \qquad (34)
\end{aligned}
$$

In these equations, the Coulomb tip friction term μK_{rub} is zero for a local rub, and is non-zero only for a rare event of full 360° contact with the case. In addition to Eqs. (33) and (34), the following additional two equations are obtained to account for the rigid body motion of the flexible shaft supported on multiple bearings:

$$
\begin{aligned}
&[(\rho A)_s\ell + M_D + N(\rho A)_b L]\ddot{U}_0 + \sum_{i=1}^{N_b}[(D_{xx}^b)_i + NC_t]\dot{U}_0 + \left[\sum_{i=1}^{N_b}(S_{xx}^b)_i + K_{rub}\right]U_0\\
&\quad+\left[\sum_{i=1}^{N_b}(D_{xy}^b)_i\right]\dot{V}_0 + \left[\sum_{i=1}^{N_b}(S_{xy}^b)_i + \mu K_{rub}\right]V_0\\
&\quad+\sum_{m=1}^{\infty}\left[(\rho A)_s\int_0^{\ell} W_m\,\mathrm{d}z + M\right]\ddot{U}_m + \sum_{m=1}^{\infty}\left[\sum_{i=1}^{N_b}(D_{xx}^b)_i W_m(z_i)\right]\dot{U}_m\\
&\quad+\sum_{m=1}^{\infty}\left[\sum_{i=1}^{N_b}(S_{xx}^b)_i W_m(z_i) + (B_{xx}^b)_i W_m''(z_i) + K_{rub}W_m(\ell) + P(t)W_m'(\ell)\right]U_m
\end{aligned}
$$

$$
\begin{aligned}
&+\sum_{m=1}^{\infty}\left[\sum_{i=1}^{N_b}(D^b_{xy})_i W_m(z_i)\right]\dot{V}_m+\sum_{m=1}^{\infty}\left[\sum_{i=1}^{N_b}(S^b_{xy})_i W_m(z_i)+\mu K_{rub}W_m(\ell)\right]V_m\\
&-(\rho A)_b L\sum_{j=1}^{N}\sin\left(\frac{2\pi j}{N}\right)(\ddot{X}_q)_j\\
&+\sum_{j=1}^{N}\left[-\left[\sum_{i=1}^{N_b}(D^b_{xx})_i+C_t\right]\cos\beta\sin\left(\frac{2\pi j}{N}\right)+\left[\sum_{i=1}^{N_b}(D^b_{yx})_i\right]\cos\beta\cos\left(\frac{2\pi j}{N}\right)\right](\dot{X}_q)_j\\
&+\sum_{j=1}^{N}\begin{bmatrix}-(EI)_b Y'''_q(0)\sin\left(\frac{2\pi j}{N}-\beta\right)-\pi^2\Omega^2(\rho A)_b\sin\left(\frac{2\pi j}{N}-\beta\right)[(R+r)/2]\\ -\left[\sum_{i=1}^{N_b}(S^b_{xx})_i+K_{rub}\right]\cos\beta\sin\left(\frac{2\pi j}{N}\right)+\left[\sum_{i=1}^{N_b}(S^b_{yx})_i+\mu K_{rub}\right]\cos\beta\cos\left(\frac{2\pi j}{N}\right)\end{bmatrix}(X_q)_j\\
&=F_U\cos(\theta+\phi)+\sum_{j=1}^{N}(F_a)_j\cos\left(\frac{2\pi j}{N}+\theta\right),
\end{aligned}
\tag{35}
$$

$$
\begin{aligned}
&\left[\sum_{i=1}^{N_b}(D^b_{yx})_i\right]\dot{U}_0+\left[\sum_{i=1}^{N_b}(S^b_{yx})_i-\mu K_{rub}\right]U_0\\
&+[(\rho A)_s\ell+M_D+N(\rho A)_b L]\ddot{V}_0+\sum_{i=1}^{N_b}[(D^b_{yy})_i+NC_t]\dot{V}_0+\left[\sum_{i=1}^{N_b}(S^b_{yy})_i+K_{rub}\right]V_0\\
&+\sum_{m=1}^{\infty}\left[\sum_{i=1}^{N_b}(D^b_{yx})_i W_m(z_i)\right]\dot{U}_m+\sum_{m=1}^{\infty}\left[\sum_{i=1}^{N_b}(S^b_{yx})_i W_m(z_i)-\mu K_{rub}W_m(\ell)\right]U_m\\
&+\sum_{m=1}^{\infty}\left[(\rho A)_s\int_0^{\ell}W_m\,\mathrm{d}z+M\right]\ddot{V}_m+\sum_{m=1}^{\infty}\left[\sum_{i=1}^{N_b}(D^b_{yy})_i W_m(z_i)\right]\dot{V}_m\\
&+\sum_{m=1}^{\infty}\left[\sum_{i=1}^{N_b}(S^b_{yy})_i W_m(z_i)+(B^b_{yy})_i W''_m(z_i)+K_{rub}W_m(\ell)+P(t)W'_m(\ell)\right]V_m\\
&+(\rho A)_b L\sum_{j=1}^{N}\cos\left(\frac{2\pi j}{N}\right)(\ddot{X}_q)_j\\
&+\sum_{j=1}^{N}\left[-\left[\sum_{i=1}^{N_b}(D^b_{xy})_i\right]\cos\beta\sin\left(\frac{2\pi j}{N}\right)+\left[\sum_{i=1}^{N_b}(D^b_{yy})_i+C_t\right]\cos\beta\cos\left(\frac{2\pi j}{N}\right)\right](\dot{X}_q)_j\\
&+\sum_{j=1}^{N}\begin{bmatrix}-(EI)_b Y'''_n(0)\cos\left(\frac{2\pi j}{N}-\beta\right)+\pi^2\Omega^2(\rho A)_b\cos\left(\frac{2\pi j}{N}-\beta\right)[(R+r)/2]\\ -\left[\sum_{i=1}^{N_b}(S^b_{xy})_i-\mu K_{rub}\right]\cos\beta\sin\left(\frac{2\pi j}{N}\right)+\left[\sum_{i=1}^{N_b}(S^b_{yy})_i+K_{rub}\right]\cos\beta\cos\left(\frac{2\pi j}{N}\right)\end{bmatrix}(X_q)_j\\
&=F_U\sin(\theta+\phi)+\sum_{j=1}^{N}(F_a)_j\sin\left(\frac{2\pi j}{N}+\theta\right).
\end{aligned}
\tag{36}
$$

Eqs. (34)–(36) represent the equations of motion for the shaft, and each N number of Eq. (12) represent the equation of motion for individual blades. As an example, we will solve here the dynamic stability of an overhung rotor supported on multiple bearings, namely, the bearing no. 1 located axially at $z = z_1 = 0$, the bearing no. 2 at $z = z_2$ and so on. The general equation of motion for the entire rotor shaft including all the blades in a matrix form can be written as

$$[\boldsymbol{M}]\{\ddot{\boldsymbol{f}}\} + [\boldsymbol{C}]\{\dot{\boldsymbol{f}}\} + [\boldsymbol{K}(t)]\{\boldsymbol{f}\} = \{\boldsymbol{F}(t)\}. \tag{37}$$

Here, time-dependence of the stiffness matrix outlines the non-linear characteristics of the equation of motion. The inertia matrix $[\boldsymbol{M}]$ is always symmetric, however, the velocity-dependent matrix $[\boldsymbol{C}]$ is a combination of symmetric and skew-symmetric matrix. If the damping in the bearing $[\boldsymbol{D}]_b$ is not symmetrical then, in general, it can be any matrix. The skew-symmetric terms is due to gyroscopic effect in a spinning rotor. The displacement-dependent matrix $[\boldsymbol{K}]$ can have time-dependent term due to non-linearity. In a simple linear structure, it will be a symmetric matrix, however, due to material internal damping terms and torque in the rotor, it will have skew-symmetric terms. Moreover, due to the contact–impact load with the outer case, it will have time-dependent non-linear terms. Hence, the matrix terms used in Eq. (37) can be broken into following separate matrices.

$$[\boldsymbol{M}]\{\ddot{\boldsymbol{f}}\} + [[\boldsymbol{C}]_D + [\boldsymbol{C}]_G]\{\dot{\boldsymbol{f}}\} + ([[\boldsymbol{K}]_S + [\boldsymbol{K}]_I] - [[\boldsymbol{B}]_1 + [\boldsymbol{B}]_2]\psi(t))\{\boldsymbol{f}\} = \{\boldsymbol{F}(t)\}, \tag{38}$$

where $[\boldsymbol{M}]$ is the mass matrix (symmetrical), $[\boldsymbol{C}]_D$ the damping matrix (symmetrical or non-symmetrical depending upon the bearing), $[\boldsymbol{C}]_G$ the gyroscopic matrix (skew-symmetric, causes forward and backward whirl in the shaft), $[\boldsymbol{K}]_S$ the stiffness matrix (generally symmetrical, but may be non-symmetrical due to non-symmetrical bearing in the horizontal and vertical directions), $[\boldsymbol{K}]_I$ the instability matrix (skew-symmetric caused by the internal damping in the shaft and also torque in the system), $[\boldsymbol{B}]_1$ the time-dependent stiffness matrix (generally symmetrical and causes parametric resonance due to the radial load on the blade tip and also due to axial load on the shaft), $[\boldsymbol{B}]_2$ the time-dependent stiffness matrix (skew-symmetric and causes parametric instability in the shaft, due to fluctuating torque in the system), and $\{\boldsymbol{F}(t)\}$ the column vector containing external forces on the dynamical system.

It can be seen that in Eq. (37) the terms containing generalized co-ordinates in the column-vector $\{\boldsymbol{f}(t)\}$ have dimensions of length. Suppose, we consider 'm' number of modes on the shaft and 'n' number of modes for each blade, then for brevity we can introduce the following notations for the generalized co-ordinates $\{\boldsymbol{f}(t)\}$.

Rotor deflections:

$$f_1(t) = U_0(t), \quad f_3(t) = U_1(t), \quad f_5(t) = U_2(t), \quad f_{1+2m}(t) = U_m(t),$$

$$f_2(t) = V_0(t), \quad f_4(t) = V_1(t), \quad f_6(t) = V_2(t), \quad f_{2+2m}(t) = V_m(t).$$

Blade deflections:

$$\text{1st Blade} : f_{3+2m}(t) = (X_1(t))_1,\ f_{4+2m}(t) = (X_2(t))_1 \ldots,\ f_{n+2+2m}(t) = (X_n(t))_1.$$

$$\text{2nd Blade} : f_{n+3+2m}(t) = (X_1(t))_2,\ f_{n+4+2m}(t) = (X_2(t))_2 \ldots,\ f_{2n+2+2m}(t) = (X_n(t))_2.$$

$$\text{3rd Blade}: f_{2n+3+2m}(t) = (X_1(t))_3,\ f_{2n+4+2m}(t) = (X_2(t))_3 \ldots,\ f_{3n+2+2m}(t) = (X_n(t))_3.$$

$$\vdots$$

$$j\text{th Blade}: f_{(j-1)n+3+2m}(t) = (X_1(t))_j,\ f_{(j-1)n+4+2m}(t) = (X_2(t))_j \ldots,\ f_{jn+2+2m}(t) = (X_n(t))_j.$$

$$(N-1)\text{th Blade}: f_{(N-2)n+3+2m}(t) = (X_1(t))_{N-1},\ f_{(N-2)n+4+2m}(t) = (X_2(t))_{N-1} \ldots,$$
$$f_{(N-1)n+2+2m}(t) = (X_n(t))_{N-1}.$$

$$N\text{th Blade}: f_{(N-1)n+3+2m}(t) = (X_1(t))_N,\ f_{(N-1)n+4+2m}(t) = (X_2(t))_N \ldots,$$
$$f_{Nn+2+2m}(t) = (X_n(t))_N.$$

In the above notation for the X terms, the first index refers to the mode shape number for the blade and the second index is the corresponding blade number. Thus, $\{\boldsymbol{f}\}^{\mathrm{T}} = \{f_1\ f_2\ f_3\ f_4\ f_5\ f_6\ f_7\ f_8\ \ldots\ f_{nN+2+2m}\}$ and $(\cdot)$ denotes derivative with respect to time 't'. The non-zero terms of the matrices $[\boldsymbol{M}]$, $[\boldsymbol{C}]$, $[\boldsymbol{K}]$ and $[\boldsymbol{B}]$ are

$$[K_{1,1}] = \left[\sum_{i=1}^{N_b} (S^b_{xx})_i + K_{rub}\right], \quad [K_{1,2}] = \left[\sum_{i=1}^{N_b} (S^b_{xy})_i + \mu K_{rub}\right],$$

$$[K_{2,1}] = \left[\sum_{i=1}^{N_b} (S^b_{yx})_i - \mu K_{rub}\right], \quad [K_{2,2}] = \left[\sum_{i=1}^{N_b} (S^b_{yy})_i + K_{rub}\right],$$

$$[K_{2m+1,1}] = \left[\sum_{i=1}^{N_b} (S^b_{xx})_i W_m(z_i) + (B^b_{xx})_i W''_m(z_i) + K_{rub} W_m(\ell) + P(t) W'_m(\ell)\right],$$

$$[K_{2m+1,2}] = \left[\sum_{i=1}^{N_b} (S^b_{xy})_i W_m(z_i) + \mu K_{rub} W_m(\ell)\right], \quad [K_{2m+2,1}] = \left[\sum_{i=1}^{N_b} (S^b_{yx})_i W_m(z_i) - \mu K_{rub} W_m(\ell)\right],$$

$$[K_{2m+2,2}] = \left[\sum_{i=1}^{N_b} (S^b_{yy})_i W_m(z_i) + (B^b_{yy})_i W''_m(z_i) + K_{rub} W_m(\ell) + P(t) W'_m(\ell)\right],$$

$$[K_{2m+1,2q+1}] = (EI)_s \left[\int_0^\ell W''''_q W_m \,\mathrm{d}z - W'''_q(\ell) W_m(\ell)\right] - P(t)\left[\int_0^\ell W''_q W_m \,\mathrm{d}z - W'_q(\ell) W_m(\ell)\right]$$
$$+ \sum_{i=1}^{N_b} [(S^b_{xx})_i W_q(z_i) W_m(z_i) + (B^b_{xx})_i W''_q(z_i) W_m(z_i)] + K_{rub} W_m(\ell) W_q(\ell),$$

$$[K_{2m+2,2q+2}] = (EI)_s \left[\int_0^\ell W''''_q W_m \,\mathrm{d}z - W'''_q(\ell) W_m(\ell)\right] - P(t)\left[\int_0^\ell W''_q W_m \,\mathrm{d}z - W'_q(\ell) W_m(\ell)\right]$$
$$+ \sum_{i=1}^{N_b} [(S^b_{yy})_i W_q(z_i) W_m(z_i) + (B^b_{yy})_i W''_q(z_i) W_m(z_i)] + K_{rub} W_m(\ell) W_q(\ell),$$

$$[K_{2m+1,2q+2}] = 2\zeta H\Omega \int_0^\ell W_q'''' W_m \,\mathrm{d}z + T(t)\left[\int_0^\ell W_q'''' W_m \,\mathrm{d}z - W_q'(\ell)W_m'(\ell)\right] + \mu K_{rub}(W_m(\ell)W_q(\ell) - eRW_q'(\ell)W_m(\ell)) + \sum_{i=1}^{N_b}(S_{xy}^b)_i W_m(z_i)W_q(z_i),$$

$$[K_{2m+2,2q+1}] = -2\zeta H\Omega \int_0^\ell W_q'''' W_m \,\mathrm{d}z - T(t)\left[\int_0^\ell W_q'''' W_m \,\mathrm{d}z - W_q'(\ell)W_m'(\ell)\right] - \mu K_{rub}(W_q(\ell)W_m(\ell) - eRW_q'(\ell)W_m(\ell)) + \sum_{i=1}^{N_b}(S_{yx}^b)_i W_m(z_i)W_q(z_i).$$

Skew-symmetric non-diagonal terms of the stiffness matrix $[\boldsymbol{K}]$ are

$$[K_{2m+2,2n+1}] = -[K_{2n+1,2m+2}], \quad [K_{2m+1,2n+2}] = -[K_{2n+2,2m+1}].$$

Symmetric non-diagonal terms of the stiffness matrix $[\boldsymbol{K}]$ are

$$[K_{2m+1,2n+1}] = [K_{2n+1,2m+1}], \quad [K_{2m+2,2n+2}] = [K_{2n+2,2m+2}],$$

$$[M_{1,1}] = [M_{2,2}] = N(\rho A)_b L + M_D + (\rho A)_s \ell,$$

$$[M_{1,2m+1}] = [M_{2m+1,1}] = \left[(\rho A)_s \int_0^\ell W_m \,\mathrm{d}z + M\right],$$

$$[M_{2,2m+2}] = [M_{2m+2,2}] = \left[(\rho A)_s \int_0^\ell W_m \,\mathrm{d}z + M\right],$$

$$[M_{2q+1,2m+1}] = (\rho A)_s \int_0^\ell W_m W_q \,\mathrm{d}z - I_d \int_0^\ell W_m'' W_q \,\mathrm{d}z + JW_m'(\ell)W_q'(\ell) + MW_m(\ell)W_q(\ell),$$

$$[M_{2n+2,2m+2}] = (\rho A)_s \int_0^\ell W_m W_n \,\mathrm{d}z - I_d \int_0^\ell W_m'' W_n \,\mathrm{d}z + JW_m'(\ell)W_n'(\ell) + MW_m(\ell)W_n(\ell),$$

$$[C_{1,1}] = N_r C_t + \left[\sum_{i=1}^{N_b}(D_{xx}^b)_i\right].$$

Here, N_r represents the number of blades which are rubbing at any given instant.

$$[C_{1,2}] = \sum_{i=1}^{N_b}(D_{xy}^b)_i, \quad [C_{2,1}] = \sum_{i=1}^{N_b}(D_{yx}^b)_i, \quad [C_{2,2}] = N_r C_t + \sum_{i=1}^{N_b}(D_{yy}^b)_i,$$

$$[C_{1,2m+1}] = \sum_{i=1}^{N_b}(D_{xx}^b)_i W_m(z_i), \quad [C_{2,2m+1}] = \sum_{i=1}^{N_b}(D_{yx}^b)_i W_m(z_i), \quad [C_{1,2m+2}] = \sum_{i=1}^{N_b}(D_{xy}^b)_i W_m(z_i),$$

$$[C_{2,2m+2}] = \sum_{i=1}^{N_b}(D_{yy}^b)_i W_m(z_i), \quad [C_{2m+1,1}] = \sum_{i=1}^{N_b}(D_{xx}^b)_i W_m(z_i), \quad [C_{2m+1,2}] = \sum_{i=1}^{N_b}(D_{xy}^b)_i W_m(z_i),$$

$$[C_{2m+2,1}] = \sum_{i=1}^{N_b} (D^b_{yx})_i W_m(z_i), \quad [C_{2m+2,2}] = \sum_{i=1}^{N_b} (D^b_{yy})_i W_m(z_i),$$

$$[C_{2q+1,2m+1}] = 2\zeta H \int_0^\ell W''''_m W_q \, \mathrm{d}z + \sum_{i=1}^{N_b} (D^b_{xx})_i W_m(z_i) W_q(z_i),$$

$$[C_{2q+2,2m+2}] = 2\zeta H \int_0^\ell W''''_m W_q \, \mathrm{d}z + \sum_{i=1}^{N_b} (D^b_{yy})_i W_m(z_i) W_q(z_i),$$

$$[C_{2q+1,2m+2}] = -2I_d\Omega \int_0^\ell W''_m W_q \, \mathrm{d}z + 2J_D\Omega W'_m(\ell) W'_q(\ell) + \sum_{i=1}^{N_b} (D^b_{xy})_i W_m(z_i) W_q(z_i),$$

$$[C_{2m+2,2q+1}] = 2I_d\Omega \int_0^\ell W''_m W_q \, \mathrm{d}z - 2J_D\Omega W'_m(\ell) W'_q(\ell) + \sum_{i=1}^{N_b} (D^b_{yx})_i W_m(z_i) W_q(z_i),$$

$$[C_{2q+2,2m+1}] = 2I_d\Omega \int_0^\ell W''_m W_q \, \mathrm{d}z - 2J_D\Omega W'_m(\ell) W'_q(\ell) + \sum_{i=1}^{N_b} (D^b_{yx})_i W_m(z_i) W_q(z_i),$$

$$[C_{2m+1,2q+2}] = -2I_d\Omega \int_0^\ell W''_m W_q \, \mathrm{d}z + 2J_D\Omega W'_m(\ell) W'_q(\ell) + \sum_{i=1}^{N_b} (D^b_{xy})_i W_m(z_i) W_q(z_i),$$

$$[M_{(j-1)n+3+2m,1}]_x = -M_b \sin\left(\frac{2\pi j}{N}\right), \quad [M_{(j-1)n+3+2m,2}]_y = M_b \cos\left(\frac{2\pi j}{N}\right),$$

$$[M_{(j-1)n+3+2m,3}]_x = -(\rho A)_b \sin\left(\frac{2\pi j}{N}\right)\left[\sum_{q=1} W_1(\ell) \int_0^L Y_1(s)\,\mathrm{d}s + W'_1(\ell)\cos^2\left(\frac{2\pi j}{N}\right) \int_0^L Y'_1(s)(s+r)^2 \,\mathrm{d}s\right],$$

$$[M_{(j-1)n+3+2m,4}]_y = (\rho A)_b \cos\left(\frac{2\pi j}{N}\right)\left[\sum_{q=1} W_1(\ell) \int_0^L Y_1(s)\,\mathrm{d}s + W'_1(\ell)\sin^2\left(\frac{2\pi j}{N}\right) \int_0^L Y'_1(s)(s+r)^2 \,\mathrm{d}s\right],$$

$$\vdots$$

$$[M_{(j-1)n+3+2m,1+2m}]_x = -(\rho A)_b \sin\left(\frac{2\pi j}{N}\right)\left[\sum_{q=1} W_m(\ell)\int_0^L Y_1(s)\,\mathrm{d}s + W'_m(\ell)\cos^2\left(\frac{2\pi j}{N}\right)\int_0^L Y'_1(s)(s+r)^2\,\mathrm{d}s\right],$$

$$[M_{(j-1)n+3+2m,2+2m}]_y = (\rho A)_b \cos\left(\frac{2\pi j}{N}\right)\left[\sum_{q=1} W_m(\ell)\int_0^L Y_1(s)\,\mathrm{d}s + W'_m(\ell)\sin^2\left(\frac{2\pi j}{N}\right)\int_0^L Y'_1(s)(s+r)^2\,\mathrm{d}s\right],$$

$$[M_{(j-1)n+3+2m,(j-1)n+3+2m}] = (\rho A)_b\left[\int_0^L Y_1 Y_1\,\mathrm{d}s\right],$$

$$[M_{(j-1)n+3+2m,(j-1)n+4+2m}] = (\rho A)_b\left[\int_0^L Y_1 Y_2\,\mathrm{d}s\right],$$

$$[M_{(j-1)n+3+2m,jn+2+2m}] = (\rho A)_b\left[\int_0^L Y_1 Y_n\,\mathrm{d}s\right],$$

$$[K_{(j-1)n+3+2m,1}]_x = \begin{bmatrix} -(EI)_b Y'''_1(0)\sin\left(\frac{2\pi j}{N}-\beta\right) - \pi^2\Omega^2(\rho A)_b \sin\left(\frac{2\pi j}{N}-\beta\right)[(R+r)/2] \\ -\left[\sum_{i=1}^{N_b}(S^b_{xx})_i + K_{rub}\right]\cos\beta\sin\left(\frac{2\pi j}{N}\right) + \left[\sum_{i=1}^{N_b}(S^b_{yx})_i - \mu K_{rub}\right]\cos\beta\cos\left(\frac{2\pi j}{N}\right) \end{bmatrix},$$

$$[K_{(j-1)n+3+2m,2}]_y = \begin{bmatrix} -(EI)_b Y'''_1(0)\cos\left(\frac{2\pi j}{N}-\beta\right) + \pi^2\Omega^2(\rho A)_b \cos\left(\frac{2\pi j}{N}-\beta\right)[(R+r)/2] \\ -\left[\sum_{i=1}^{N_b}(S^b_{xy})_i + \mu K_{rub}\right]\cos\beta\sin\left(\frac{2\pi j}{N}\right) + \left[\sum_{i=1}^{N_b}(S^b_{yy})_i + K_{rub}\right]\cos\beta\cos\left(\frac{2\pi j}{N}\right) \end{bmatrix},$$

$$[K_{(j-1)n+3+2m,3}]_x = \begin{bmatrix} -(EI)_b Y'''_1(0)W_1(\ell) + (EI)_b Y''_1(0)W'_1(\ell) \\ -(EI)_s W'''_1(\ell) - \pi^2\Omega^2(\rho A)_b W_1(\ell)[(R+r)/2] \end{bmatrix}\sin\left(\frac{2\pi j}{N}-\beta\right),$$

$$[K_{(j-1)n+3+2m,4}]_y = \begin{bmatrix} -(EI)_b Y'''_1(0)W_1(\ell) + (EI)_b Y''_1(0)W'_1(\ell) \\ -(EI)_s W'''_1(\ell) + \pi^2\Omega^2(\rho A)_b W_1(\ell)[(R+r)/2] \end{bmatrix}\cos\left(\frac{2\pi j}{N}-\beta\right),$$

$$[K_{(j-1)n+3+2m,1+2m}]_x = \begin{bmatrix} -(EI)_b Y'''_1(0)W_m(\ell) + (EI)_b Y''_1(0)W'_m(\ell) \\ -(EI)_s W'''_m(\ell) - \pi^2\Omega^2(\rho A)_b W_m(\ell)[(R+r)/2] \end{bmatrix}\sin\left(\frac{2\pi j}{N}-\beta\right),$$

$$[K_{(j-1)n+3+2m,2+2m}]_y = \begin{bmatrix} -(EI)_b Y_1'''(0) W_m(\ell) + (EI)_b Y_1''(0) W_m'(\ell) \\ -(EI)_s W_m'''(\ell) + \pi^2 \Omega^2 (\rho A)_b W_m(\ell)[(R+r)/2] \end{bmatrix} \cos\left(\frac{2\pi j}{N} - \beta\right),$$

$$[K_{(j-1)n+3+2m,(j-1)n+3+2m}] = \begin{bmatrix} (EI)_b \int_0^L Y_1 Y_1'''' \, \mathrm{d}s + (\rho A)_b \Omega^2 \int_0^L (s+r) Y_1 Y_1' \, \mathrm{d}s \\ -\dfrac{(\rho A)_b \Omega^2}{2} \int_0^L (2rL + L^2 - 2rs - s^2) Y_1 Y_1'' \, \mathrm{d}s - (F_a(t))_j \int_0^L Y_1 Y_1'' \, \mathrm{d}s \end{bmatrix},$$

$$[K_{(j-1)n+3+2m,(j-1)n+4+2m}] = \begin{bmatrix} (EI)_b \int_0^L Y_1 Y_2'''' \, \mathrm{d}s + (\rho A)_b \Omega^2 \int_0^L (s+r) Y_1 Y_2' \, \mathrm{d}s \\ -\dfrac{(\rho A)_b \Omega^2}{2} \int_0^L (2rL + L^2 - 2rs - s^2) Y_1 Y_2'' \, \mathrm{d}s - (F_a(t))_j \int_0^L Y_1 Y_2'' \, \mathrm{d}s \end{bmatrix},$$

$$[K_{(j-1)n+3+2m,jn+2+2m}] = \begin{bmatrix} (EI)_b \int_0^L Y_1 Y_n'''' \, \mathrm{d}s + (\rho A)_b \Omega^2 \int_0^L (s+r) Y_1 Y_n' \, \mathrm{d}s \\ -\dfrac{(\rho A)_b \Omega^2}{2} \int_0^L (2rL + L^2 - 2rs - s^2) Y_1 Y_n'' \, \mathrm{d}s - (F_a(t))_j \int_0^L Y_1 Y_n'' \, \mathrm{d}s \end{bmatrix},$$

$$[C_{(j-1)n+3+2m,1}]_x = \left[-\left[\sum_{i=1}^{N_b} (D_{xx}^b)_i + C_t \right] \cos\beta \sin\left(\frac{2\pi j}{N}\right) + \left[\sum_{i=1}^{N_b} (D_{yx}^b)_i \right] \cos\beta \cos\left(\frac{2\pi j}{N}\right) \right],$$

$$[C_{(j-1)n+3+2m,2}]_y = \left[-\left[\sum_{i=1}^{N_b} (D_{xy}^b)_i \right] \cos\beta \sin\left(\frac{2\pi j}{N}\right) + \left[\sum_{i=1}^{N_b} (D_{yy}^b)_i + C_t \right] \cos\beta \cos\left(\frac{2\pi j}{N}\right) \right],$$

$$[C_{(j-1)n+3+2m,3}]_x = \begin{bmatrix} -C_t \cos\beta W_1(\ell) \sin\left(\dfrac{2\pi j}{N}\right) \int_0^L Y_1 \delta(s-L) \, \mathrm{d}s \\ -\Omega(\rho A)_b \sin\beta W_1'(\ell) \cos\left(\dfrac{2\pi j}{N}\right) \int_0^L Y_1'(s)(s+r)^2 \, \mathrm{d}s \end{bmatrix},$$

$$[C_{(j-1)n+3+2m,4}]_y = \begin{bmatrix} C_t \cos\beta W_1(\ell) \cos\left(\dfrac{2\pi j}{N}\right) \int_0^L Y_1 \delta(s-L) \, \mathrm{d}s \\ -\Omega(\rho A)_b \sin\beta W_1'(\ell) \sin\left(\dfrac{2\pi j}{N}\right) \int_0^L Y_1'(s)(s+r)^2 \, \mathrm{d}s \end{bmatrix},$$

$$[C_{(j-1)n+3+2m,1+2m}]_x = \begin{bmatrix} -C_t \cos\beta W_m(\ell) \sin\left(\dfrac{2\pi j}{N}\right) \int_0^L Y_1 \delta(s-L) \, \mathrm{d}s \\ -\Omega(\rho A)_b \sin\beta W_m'(\ell) \cos\left(\dfrac{2\pi j}{N}\right) \int_0^L Y_1'(s)(s+r)^2 \, \mathrm{d}s \end{bmatrix},$$

$$[C_{(j-1)n+3+2m,2+2m}]_y = \begin{bmatrix} C_t \cos\beta W_m(\ell) \cos\left(\dfrac{2\pi j}{N}\right) \int_0^L Y_1 \delta(s-L) \, \mathrm{d}s \\ -\Omega(\rho A)_b \sin\beta W_m'(\ell) \sin\left(\dfrac{2\pi j}{N}\right) \int_0^L Y_1'(s)(s+r)^2 \, \mathrm{d}s \end{bmatrix},$$

$$[C_{(j-1)n+3+2m,(j-1)n+3+2m}] = C_t\left[\int_0^L Y_1 Y_1 \delta(s-L)\,\mathrm{d}s\right],$$

$$[C_{(j-1)n+3+2m,(j-1)n+4+2m}] = C_t\left[\int_0^L Y_1 Y_2 \delta(s-L)\,\mathrm{d}s\right],$$

$$\vdots$$

$$[C_{(j-1)n+3+2m,\,jn+2+2m}] = C_t\left[\int_0^L Y_1 Y_n \delta(s-L)\,\mathrm{d}s\right].$$

For generating the mass, stiffness and damping matrix terms outlined above, the displacement functions are

$$Y_n(s) = a_{1n}s^3 + a_{2n}s^2 + a_{3n}s + \sin\left(\frac{(2n-1)\pi s}{2L}\right),$$

$$W_m(z) = 1 - \cos\left(\frac{(2m-1)\pi z}{2\ell}\right),$$

$$M_b = (\rho A)_b L, \quad C_t = 2\zeta_b \frac{L^2}{\pi^2}[EI\rho A]^{1/2}_{blade}.$$

In the above derivations of the blade stiffness matrix terms, it is assumed that the displacement function $Y_n(s)$ satisfies all the geometric as well as force boundary conditions. However, in the Rayleigh–Ritz method, it is not necessary to satisfy the force boundary conditions by the displacement function. Thus, if $Y_n(s)$ is limited to only geometric boundary conditions, then the typical blade stiffness matrix term should be modified as follows:

$$[K_{(j-1)n+3+2m,\,jn+2+2m}] = \begin{bmatrix} (EI)_b \int_0^L Y_1 Y_n''''\,\mathrm{d}s + (\rho A)_b \Omega^2 \int_0^L (s+r) Y_1 Y_n'\,\mathrm{d}s \\ -\dfrac{(\rho A)_b \Omega^2}{2} \int_0^L (2rL + L^2 - 2rs - s^2) Y_1 Y_n''\,\mathrm{d}s + (F_a(t))_j [Y_1(L) Y_n'(L) - \int_0^L Y_1 Y_n''\,\mathrm{d}s] \end{bmatrix}.$$

In all the above relations, M_D is the mass of the disk and M_b is the mass of each blade mounted on it, whereas $[M_{i,j}]$, with double subscripts, denotes the elements of the $[\boldsymbol{M}]$ matrix. Here, it should be noted that while $[\boldsymbol{M}]$ is a symmetric matrix, other matrices $[\boldsymbol{C}]$, $[\boldsymbol{K}]$, $[\boldsymbol{B}]$ are combinations of symmetric and skew-symmetric parts. Furthermore, terms containing dynamic coefficient of friction μ are making the non-diagonal stiffness terms skew-symmetric, which is attributed to introduce instability in the dynamical system. However, terms containing dynamic coefficient of friction μ are non-zero only for a relatively rare case of full 360° rub, hence all tip rubs are not necessarily unstable. The dynamic stability of the rotor can be determined either in a frequency-domain or in a time-domain.

The frequency-domain stability criteria can be used only for linear or quasi-linear type of dynamic problem, where it is possible to write the $[\boldsymbol{M}]$, $[\boldsymbol{C}]$, $[\boldsymbol{K}]$ and $[\boldsymbol{B}]$ matrices explicitly without any reference to the displacements such as the effect of gaps or clearances in the system. However, the frequency-domain stability conditions provide a good insight in a complex rotordynamic

problems, where whirl instability can be initiated due to the excitation of certain mode shapes in the rotor due to infrequent rubbing of blades. These instabilities which may occur at certain speed ranges of the rotor can be either a simple or parametric resonance type of instability in the flexible rotor–blade system.

In the time-domain stability determination, one uses the direct time marching-forward-integration technique, which is a preferred approach in a true non-linear dynamical problem with clearances and varying coefficients of friction as a function of speed. In this method, if the radial excursion of the rotor at certain locations such as at bearing supports, is increasing monotonically over a period of time, which can be in the range of milliseconds to seconds, then it is considered unstable. The instability is being caused because the energy being fed into the dynamical system is not being dissipated fully by the effective damping present in the flexible rotor–blade system. The direct time-integration method is problem specific and as such does not provide a generic stability conditions to be used for some other rotor. In the following section, we will discuss the stability characteristics of the flexible rotor–blade systems during different tip rub scenarios.

6. Determining rotor stability characteristics in the frequency-domain

The method for establishing the stability criteria in the frequency domain for a flexible rotor was developed and presented by the author [7,31] earlier in full detail. The method is summarized in this paper for completeness. The set of equations of motion (38) in matrix form can be written as

$$[\boldsymbol{M}]\{\ddot{\boldsymbol{f}}\} + [[\boldsymbol{C}]_D + [\boldsymbol{C}]_G]\{\dot{\boldsymbol{f}}\} + ([[\boldsymbol{K}]_S + [\boldsymbol{K}]_I] - [[\boldsymbol{B}]_1 + [\boldsymbol{B}]_2]\psi(t))\{\boldsymbol{f}\} = \{\boldsymbol{F}(t)\}.$$

Here, $\psi(t)$ can be assumed to be made up of integral multiples of the rotation speed Ω (i.e., period of the forcing frequency $= 2\pi/\Omega$). Then, from the Fourier cosine series expansion, we have

$$\psi(t) = \sum_{q=1,2,3..}^{\infty} c_q \cos(q\Omega t),$$

where

$$c_q = \frac{\int_0^T \psi(t)\cos(q\Omega t)\,\mathrm{d}t}{\int_0^T \cos^2(q\Omega t)\,\mathrm{d}t}.$$

Thus, Eq. (38) for any particular harmonic of the rotational speed Ω can be written as

$$[\boldsymbol{M}]\{\ddot{\boldsymbol{f}}\} + [[\boldsymbol{C}]_D + [\boldsymbol{C}]_G]\{\dot{\boldsymbol{f}}\} + ([[\boldsymbol{K}]_S + [\boldsymbol{K}]_I] - [[\boldsymbol{B}]_1 + [\boldsymbol{B}]_2]\cos(q\Omega t))\{\boldsymbol{f}(t)\} = \{\boldsymbol{F}(t)\}. \quad (39)$$

Eq. (39) can be identified as a set of modified coupled Mathieu–Hill equations with additional contributions from the velocity-dependent coefficient matrix $[\boldsymbol{C}]$. It can be seen that the skew-symmetric part of the $[\boldsymbol{K}]$ matrix contains hysteretic damping H in the shaft material and the tangential torque T_0 causing instability in the dynamical system. Furthermore, the presence of non-zero $[\boldsymbol{B}]$ matrix creates parametric instability in the rotor. The solution of Eq. (39) is sought in the form of a product of two functions: first an exponential function with a characteristic

exponent λ and the second a periodic function with period as (i.e., $2\pi/\Omega$),

$$\{\boldsymbol{f}(t)\} = \mathrm{e}^{\lambda t}\left[\frac{\{\boldsymbol{b}_0\}}{2} + \sum_{k=1,2,3..}^{\infty} \{\boldsymbol{a}_k\}\sin(2\omega_k t) + \{\boldsymbol{b}_k\}\cos(2\omega_k t)\right], \tag{40}$$

where $\omega_k = k\Omega/4$ and where $\{\boldsymbol{a}_k\}$ and $\{\boldsymbol{b}_k\}$ are time-independent Fourier coefficients. Substitution of the series representation of $\{\boldsymbol{f}(t)\}$ shown in Eq. (39) enables us to use the method of harmonic balance. In this scheme, we collect the coefficients of $\mathrm{e}^{\lambda t}$, $\mathrm{e}^{\lambda t}\sin(2\omega_k t)$, $\mathrm{e}^{\lambda t}\cos(2\omega_k t)$, respectively, and equate them to zero. This yields the following set of homogeneous algebraic equations:

$$(\lambda^2[\boldsymbol{M}] + \lambda[\boldsymbol{C}] + [\boldsymbol{K}])\{\boldsymbol{b}_0\} - [\boldsymbol{B}]\{\boldsymbol{b}_2\} = \{0\}. \tag{41}$$

These systems of equations can be rearranged with three different matrices, namely, $[\boldsymbol{P}]$, $[\boldsymbol{Q}]$ and $[\boldsymbol{R}]$ as the coefficients of the ascending powers of λ in the form

$$([\boldsymbol{P}] + \lambda[\boldsymbol{Q}] + \lambda^2[\boldsymbol{R}])\{\boldsymbol{X}\} = \{0\}, \tag{42}$$

where the column vector $\{\boldsymbol{X}\}$ contains the unknown Fourier coefficients [32] such as $\boldsymbol{b}_0$, $\boldsymbol{a}_k$, $\boldsymbol{b}_k$, etc. The eigenvalue of Eq. (42) can be solved easily by first converting the equation into a "state" form by introducing a new column vector $\{\boldsymbol{Y}\} = \lambda\{\boldsymbol{X}\}$ as

$$\begin{bmatrix} 0 & [\boldsymbol{I}] \\ -[\boldsymbol{R}]^{-1}[\boldsymbol{P}] & -[\boldsymbol{R}]^{-1}[\boldsymbol{Q}] \end{bmatrix} \begin{Bmatrix} \{\boldsymbol{X}\} \\ \{\boldsymbol{Y}\} \end{Bmatrix} = \lambda \begin{Bmatrix} \{\boldsymbol{X}\} \\ \{\boldsymbol{Y}\} \end{Bmatrix}, \tag{43}$$

where $[\boldsymbol{I}]$ is an identity or unit matrix. The general solution of this set of equations results in eigenvalues λ with complex roots such that one can write $\lambda = \lambda_r \pm \mathrm{i}\lambda_i$, where $\mathrm{i} = \sqrt{-1}$. The positive and negative signs of the real part of the eigenvalue (λ_r) indicate the unstable and stable behaviors of the rotating system. The real and imaginary parts of the eigenvalues λ_r and λ_i enable us to determine the effective logarithmic decrement as

$$\delta = -2\pi\left[\frac{\lambda_r}{|\lambda_i|}\right]. \tag{44}$$

The dynamic system will be stable only when the effective logarithmic decrement for each mode is either zero or positive. In the dynamic stability problems, the usual interest is in identifying the unstable zones, i.e., the boundary frequencies (roots of Ω) of the "Principal Instability Region" for the system governed by the Mathieu–Hill equation (39) are determined by finding the eigenvalues of the matrix

$$\begin{bmatrix} 0 & 0 & [\boldsymbol{I}] & 0 \\ 0 & 0 & 0 & [\boldsymbol{I}] \\ 2[\boldsymbol{M}]^{-1}(2[\boldsymbol{K}] + [\boldsymbol{B}]) & 0 & 0 & -2[\boldsymbol{M}]^{-1}[\boldsymbol{C}] \\ 0 & 2[\boldsymbol{M}]^{-1}(2[\boldsymbol{K}] - [\boldsymbol{B}]) & 2[\boldsymbol{M}]^{-1}[\boldsymbol{C}] & 0 \end{bmatrix}. \tag{45}$$

Since all the matrices $[\boldsymbol{M}], [\boldsymbol{C}], [\boldsymbol{K}]$ and $[\boldsymbol{B}]$ are fully defined and $[\boldsymbol{I}]$ is the standard unit matrix, the complex eigenvalue problem described by the above matrix is easily solved by using the IMSL-EISPACK routine. By computing the roots of λ, the global conditions of the rotor stability with a known value of internal damping ζ and coefficient of friction μ can easily be determined for any

combination of P_0, P_t and T_0, T_t. The dynamic stability of a bladed-disk rotor system can also be checked in a time-domain solution by the direct-time integration scheme used in the following section.

7. Numerical solution for rotor stability in the time-domain

The transient response of a decelerating or accelerating rotor is of great interest in any rotordynamics problem. The two most common techniques for integrating the equations of motion and computing the displacement and velocity response of a dynamical system are (1) *Newmark's β-method*: it is an unconditionally stable implicit numerical scheme, which is commonly used for determining the long-term transient response in the area of structure dynamics; (2) *Fourth order Runge–Kutta Method*: it is an explicit technique and is commonly used for computing short-term transient response of non-linear dynamical problems, usually with pulse and impact type of loading.

In this paper, the above system of non-linear transient equations are solved in the time domain by a still more accurate sixth order Runge–Kutta numerical integration scheme. The equation of motion outlined in Eqs. (37a) and (37b) easily account for time-varying rotational speed, because in the Runge–Kutta method the instantaneous speed is updated continuously even at the mid-time-point. In order to apply this method, the system of equations are written as

$$M_{ij}\ddot{f}_j + C_{ij}\dot{f}_j + K_{ij}f_j = F_i - (F_{case})_i,$$

$$\ddot{f}_j = \frac{1}{M_{ij}}[F_i - (F_{case})_i - C_{ij}\dot{f}_j - K_{ij}f_j],$$

$$(\ddot{f}_j)_{t+\Delta t} = \frac{1}{M_{ij}}[(F_i)_{t+\Delta t} - (F_{case})_{i,t} - (C_{ij}\dot{f}_i)_t - (K_{ij}f_j)_t]. \tag{46}$$

In this equation, $1/M_{ij}$ represents the terms in the inverse of the $[\boldsymbol{M}]$ matrix, and the radial contact load from the rigid case $(F_{case})_i$ is determined by the penalty method, where all the radial deformation is in the blade tips, and the case acts like a rigid wall. The external force column vector $[\boldsymbol{F}]_i$ contains the terms pertaining to unbalance force components such as $(m_r\Omega^2)\cos(\theta+\phi) - (F_{case})_x, (m_r\Omega^2)\sin(\theta+\phi) - (F_{case})y, \ldots$, in the global x–y directions, and the blade tip forces due to friction $-\mu(F_a)_1\cos\beta$, $-\mu(F_a)_2\cos\beta, \ldots, -\mu(F_a)_N\cos\beta$, etc. in the local tangential directions. In the numerical integration algorithm of the non-linear equations of motion, the number of blades rubbing the case 'N_r', the radial load on these blades $(F_a)_j$ and the corresponding coefficient of friction μ are updated according to the direction of instantaneous velocity of the tip of the respective blades. During the time-marching forward solution, the computer program also keeps track of the bearing loads, and if any of the bearings generate higher loads than its load carrying capacity, it is considered failed at that instant and is taken out of the analysis from then onwards. The velocity $(\dot{f}_i)_{t+\Delta t}$, and displacement $(f_i)_{t+\Delta t}$ terms in a finite-difference form may be written as

$$(\dot{f}_i)_{t+\Delta t} = (\dot{f}_i)_t + \Delta t(\ddot{f}_i)_{t+\Delta t},$$

$$(f_i)_{t+\Delta t} = (f_i)_t + \Delta t\frac{(\dot{f}_i)_{t+\Delta t} + (\dot{f}_i)_t}{2} + \tfrac{1}{2}(\Delta t)^2(\ddot{f}_i)_{t+\Delta t}.$$

The initial conditions for the integration are established by determining the steady state forced harmonic response for a nominal, rotating unbalance load vector. The harmonic response (displacement) '$\boldsymbol{f}$' for a force $F = F_{max}e^{i\Omega t} = (m_r\Omega^2)e^{i\Omega t}$ with an angular velocity Ω is determined by the following equations:

$$f = f_{max}e^{i(\Omega t+\Psi)}, \quad F_r = F_{max}\cos(\Omega t), \quad F_i = F_{max}\sin(\Omega t),$$

$$\begin{bmatrix} -[\boldsymbol{M}]\Omega^2 + [\boldsymbol{K}] & -[\boldsymbol{C}]\Omega \\ [\boldsymbol{C}]\Omega & -[\boldsymbol{M}]\Omega^2 + [\boldsymbol{K}] \end{bmatrix} \begin{Bmatrix} \{\boldsymbol{f}_r\} \\ \{\boldsymbol{f}_i\} \end{Bmatrix} = \begin{Bmatrix} \{m_r\Omega^2\} \\ \{-m_r\Omega^2\} \end{Bmatrix}. \tag{47}$$

The phase difference for each mode with respect to the rotating unbalance load vector 'ψ' is written as $\psi = \tan^{-1}[\boldsymbol{f}_i/\boldsymbol{f}_r]$.

The sample numerical results are generated for a typical fan rotor with parameters listed in Table 1. For the numerical results, all linear dimensions are non-dimensionalized with respect to the blade tip radius of $R = 150$ cm, and the forces are normalized with respect to the radial force produced by 1 g (unit mass) unbalance at the outer radius.

7.1. Steady state response

The numerical scheme for computing the mass and stiffness matrices is verified and checked by determining the eigenvalues of a cantilever hollow cylindrical shaft with a rigid disk mounted at the free-end (see Fig. 4). Eqs. (33)–(36) are easily reduced to the more familiar form for a cantilever shaft, rotating at constant angular velocity of Ω, of span-length ℓ mounted with a free-end rigid disk (disk mass $= M_D$ and diametral mass moment of inertia as J_D):

$$\begin{aligned} &\sum_{m=1}^{\infty}\left[(\rho A)_s\int_0^{\ell} W_m W_n\,\mathrm{d}z + J_D W'_m(\ell)W'_n(\ell) + M_D W_m(\ell)W_n(\ell)\right]\ddot{U}_m \\ &\quad + \sum_{m=1}^{\infty}\begin{bmatrix}(EI)_s\int_0^{\ell} W''''_m W_n\,\mathrm{d}z - (EI)_s W'''_m(\ell)W_n(\ell) \\ +K_{rub}W_m(\ell)W_n(\ell)\end{bmatrix}U_m \\ &\quad + \sum_{m=1}^{\infty}[2J_D\Omega W'_m(\ell)W'_n(\ell)]\dot{V}_m + \sum_{m=1}^{\infty}[\mu K_{rub}[W_m(\ell)W_n(\ell) - eRW'_m(\ell)W_n(\ell)]]V_m \\ &\quad = F_U\left[W_n(\ell) + W'_n(\ell)\frac{D_L}{2}\right]\cos(\Omega t), \end{aligned} \tag{48a}$$

$$\begin{aligned} &\sum_{m=1}^{\infty}[-2J_D\Omega W'_m(\ell)W'_n(\ell)]\dot{U}_m - \sum_{m=1}^{\infty}[\mu K_{rub}[W_m(\ell)W_n(\ell) - eRW'_m(\ell)W_n(\ell)]]U_m \\ &\quad + \sum_{m=1}^{\infty}\left[(\rho A)_s\int_0^{\ell} W_m W_n\,\mathrm{d}z + J_D W'_m(\ell)W'_n(\ell) + M_D W_m(\ell)W_n(\ell)\right]\ddot{V}_m \\ &\quad + \sum_{m=1}^{\infty}\begin{bmatrix}(EI)_s\int_0^{\ell} W''''_m W_n\,\mathrm{d}z - (EI)_s W'''_m(\ell)W_n(\ell) \\ +K_{rub}W_m(\ell)W_n(\ell)\end{bmatrix}V_m \\ &\quad = F_U\left[W_n(\ell) + W'_n(\ell)\frac{D_L}{2}\right]\sin(\Omega t). \end{aligned} \tag{48b}$$

Table 1
Details of the parameters considered for the sample rotor used in the discussion

M_b	Mass of one blade	10 kg
M_D	Mass of the disk	150 kg
D_L	Axial length of the rigid disk	25 cm
R	Blade tip radius	150 cm
r	Blade root radius = disk outer radius	50 cm
L	Blade length	100 cm
$(A)_b$	Blade cross-sectional area	5000 mm^2
$(I)_b$	Blade area moment of inertia	0.5E6 mm^4
K_{rub}	Case filler material stiffness	10 MN/m
ℓ	Length of the shaft	350 cm
r_o	Outside radius of the shaft	7.0 cm
r_i	Inside radius of the shaft	5.5 cm
$(\rho)_s$	Mass density of the shaft material	7.833 g/cm^3
β	Blade stagger angle at the tip	60°
Speed		3000 r.p.m.
Ω	Rotor initial steady state spin velocity (rad/s)	314.159 rad/s
m_r	Mass moment of unbalance about engine axis	1E6 g cm
ϕ	Circumferential location of the unbalance at time 't' = 0 (constant)	0
N	Number of blades on the rotor	28
N_b	Number of discrete bearings supporting the shaft	3
z_i	Bearing support locations	0,300 cm, 325 cm
μ_{static}	Static coefficient of friction between the blade tip and the outer case inner surface	0.1
μ_{dyn}	Dynamic coefficient of friction between the blade tip and the outer case inner surface	0.01
$(E)_s$	Elastic Young's modulus of the rotor shaft material	200 GPa
$(E)_b$	Elastic Young's modulus of the blade material	117 GPa
c	Blade chord	35 cm

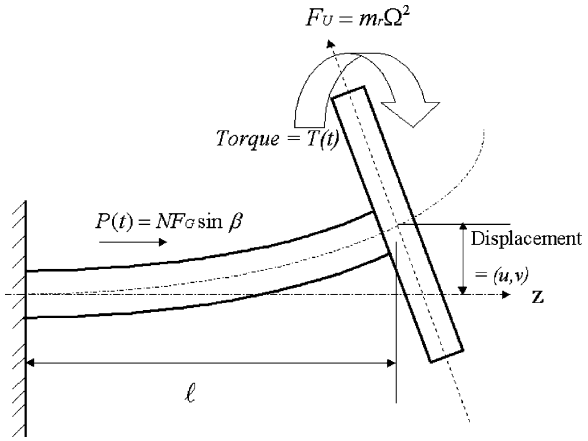

Fig. 4. External forces and the first flex deformation of the cantilever shaft with rigid disk: flexural rigidity of the shaft = $(EI)_s$, mass per unit length of the shaft = $(\rho A)_s$, mass of the disk = M_D, diametral mass moment of inertia of the disk = J_D, torque = $NF_G(r + 0.5L)\cos\beta + \sum_{j=1}^{N}(\mu F_a)_j R$.

The computed non-dimensional natural frequency parameter ξ for varying disk mass M_D are summarized in Table 2. The non-dimensional frequency parameter ξ is defined such that

$$\omega_n = \frac{\xi}{\ell^2}\sqrt{\frac{(EI)_s}{(\rho A)_s}}.$$

The computed values of ξ for the static condition matches well with closed form solution given by Harris and Crede [33]. The tabular data illustrates the fact that lower flex frequencies move down rapidly with the increasing mass, however, for higher flex modes the change is not significant. The effect of increasing mass moment of inertia of the disk 'J_D', is shown in Table 3. It is obvious that the effect of increase in 'J_D' for the lower mode is again more pronounced than for the higher modes, where the non-dimensional natural frequency parameter ξ become asymptotic very quickly.

The two system modes identified for the above rotor are: 14.86 Hz (891.5 r.p.m.) and 44.49 Hz (2669.5 r.p.m.). The typical mode shape is shown in Fig. 5. The harmonic lateral response at the bearing no. 3 support for a nominal unbalance with the rigid-disk are illustrated in Fig. 6. The effect of gyroscopic terms are plotted in Fig. 7 by listing the forward and backward whirl frequencies for the first and second flex bending modes at different rotational speeds Ω.

Before analyzing the transient response of the rotor, we have also investigated the steady state dynamic response of individual blades on this rotor during the rotating and non-rotating conditions. The dynamic buckling characteristics of each blade with its root clamped at the top of

Table 2
Computed non-dimensional frequencies ξ of a cantilever shaft with rigid overhung disk of concentrated point mass M_D

Disk-mass (M_D/Ms)	First flex	Second flex	Third flex	Fourth flex	Fifth flex	Sixth flex
0.00	3.5160	22.0351	61.7052	120.9317	199.9649	298.7559
0.10	2.9678	19.3563	55.5245	110.7328	185.4243	279.7140
0.25	2.4766	17.8520	53.0221	107.5703	181.7910	275.7414
0.50	2.0163	16.9018	51.7063	106.0816	180.1953	274.0769
0.75	1.7431	16.4846	51.1823	105.5178	179.6080	273.4753
1.00	1.5573	16.2505	50.9011	105.2217	179.3031	273.1653
2.00	1.1582	15.8613	50.4528	104.7583	178.8309	272.6872
3.00	0.9628	15.7201	50.2958	104.5986	178.6695	272.5239
4.00	0.8415	15.6472	50.2159	104.5176	178.5882	272.4415
5.00	0.7569	15.6026	50.1674	104.4687	178.5393	272.3917
6.00	0.6936	15.5727	50.1349	104.4359	178.5065	272.3579
7.00	0.6439	15.5511	50.1116	104.4124	178.4830	272.3334
8.00	0.6035	15.5348	50.0940	104.3948	178.4656	272.3154
9.00	0.5699	15.5220	50.0804	104.3810	178.4520	272.3008
10.00	0.5414	15.5119	50.0694	104.3700	178.4411	272.2888
15.00	0.4438	15.4810	50.0365	104.3368	178.4088	272.2525
35.00	0.2918	15.4455	49.9988	104.2980	178.3744	272.2000

Non-dimensional frequency factor $\xi = \omega_n \ell^2 \sqrt{\frac{(\rho A)_s}{(EI)_s}}$; shaft mass '$M_s$' $= (\rho A \ell)_s$; frequency: $\omega_n = \frac{\xi}{\ell^2}\sqrt{\frac{(EI)_s}{(\rho A)_s}}$ rad/s; $\omega_n = (\frac{1}{2\pi})\frac{\xi}{\ell^2}\sqrt{\frac{(EI)_s}{(\rho A)_s}}$ Hz.

Table 3
Effect of mass moment of inertia of the disk on the non-dimensional static frequencies ξ of a cantilever shaft with rigid overhung disk of mass M_D (For a typical value of $M_D/Ms = 15, J_D =$ diametral mass moment of inertia of the disk about its mass center)

$\frac{(J_D)}{(\rho A \ell^3)_s}$	First flex	Second flex	Third flex	Fourth flex	Fifth flex	Sixth flex
0.000	0.4438	15.4810	50.0365	104.3368	178.4088	272.2525
0.025	0.4429	10.5528	27.3565	65.3865	125.7987	207.5618
0.050	0.4421	8.2670	25.2366	64.5455	125.3496	207.2700
0.500	0.4297	2.9697	23.3562	63.8173	124.9521	207.0110
2.500	0.3753	1.5359	23.1966	63.7546	124.9166	206.9938
5.000	0.3284	1.2499	23.1767	63.7465	124.9152	206.9867
10.000	0.2654	1.0755	23.1668	63.7419	124.9148	206.9845
25.000	0.1906	0.9767	23.1603	63.7388	124.8836	206.9536
50.000	0.1456	0.9428	23.1596	63.7357	124.8525	206.9135

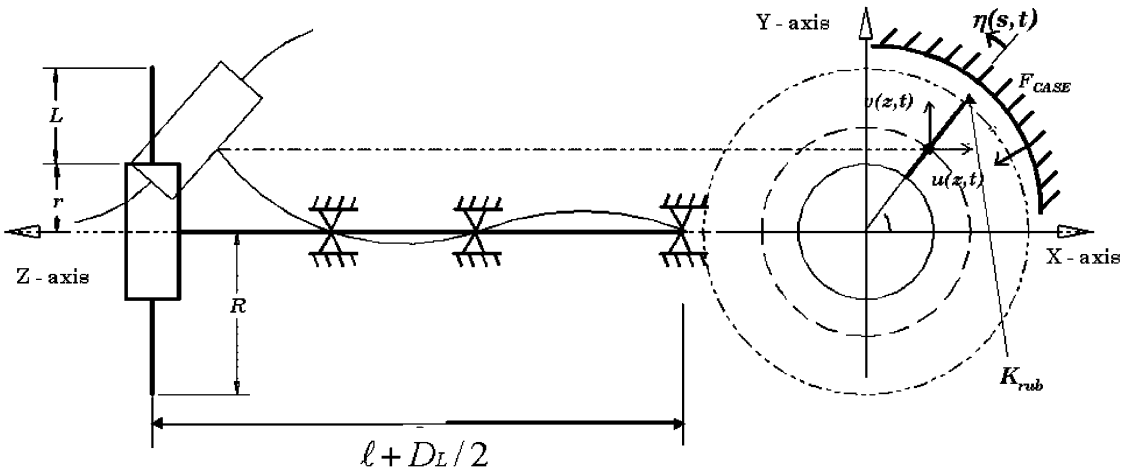

Fig. 5. A typical dynamic mode shape of a bladed rotor with multiple supports.

the disk in terms of its frequency and the critical compressive buckling load is considered in Table 4. Here, we see that the speed has significant effect on the first and second flex mode frequencies of the blade, but relatively minimal effect on the higher modes.

7.2. Transient response during deceleration through resonance

The transient response of this rotor is considered under an assumed condition of an unbalance created due to the sudden blade loss from the disk during normal operation of 3000 r.p.m. After the blade is lost the engine stalls and the rotor starts decelerating until it comes to a complete stop. During the deceleration, as the rotor passes through its resonance the disk goes through large radial excursion causing the blades to rub momentarily against the outer case. The transient

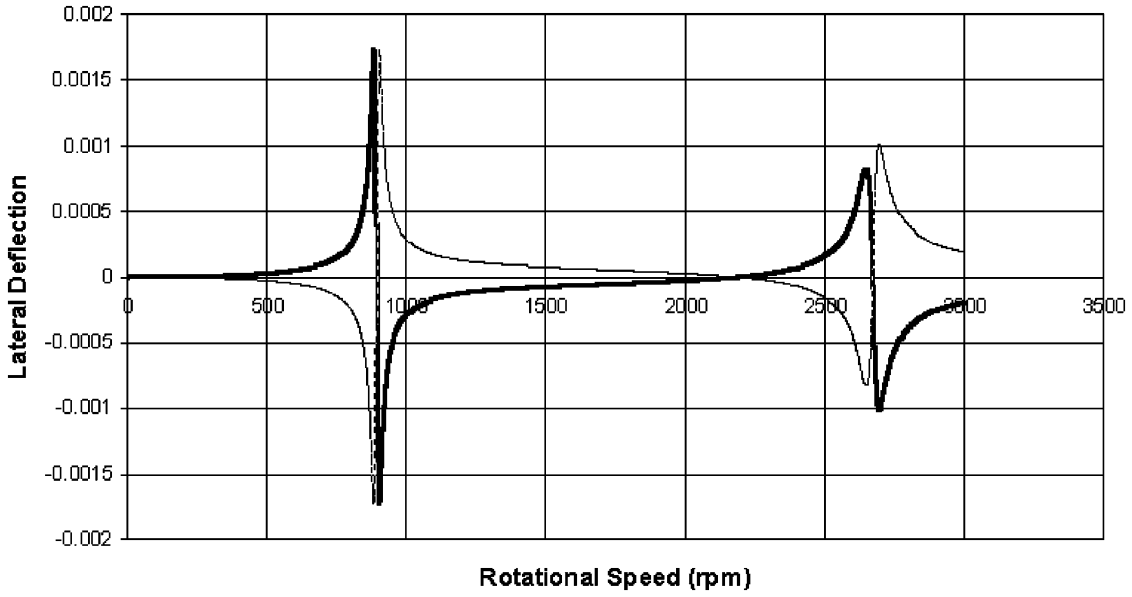

Fig. 6. Harmonic response (u, v) of the rotor at bearing no. 3 support for a nominal unbalance (——, u; ——, v).

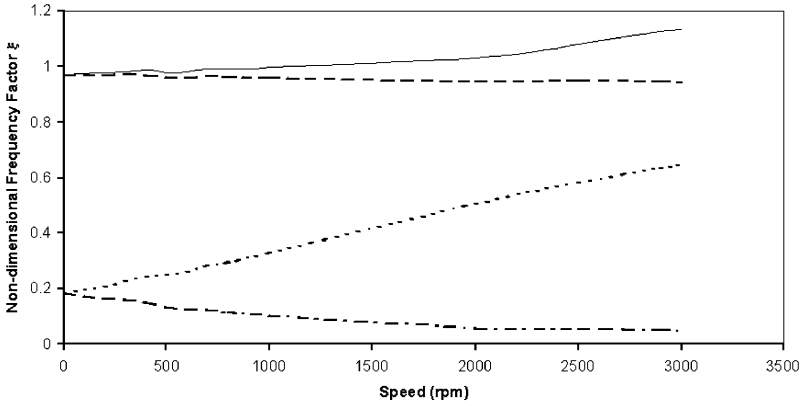

Fig. 7. Campbell diagram showing gyroscopic effect of the polar mass moment of inertia of the disk and blades on the rotor shaft natural frequency for a typical case of $M_D/M_s = 15$ with ratio of the disk/shaft polar inertia = 50 [– – –, forward whirl (first flex); — · — · —, backward whirl (first flex); ——, forward whirl (second flex); ———, backward whirl (second flex)].

response of this rotor for a typical blade-loss condition is analyzed by numerically solving the coupled equations of motion (46). The computed vertical dynamic response of the bearing no. 3 is shown in Fig. 8.

It can be seen that the peak dynamic response during deceleration does not occur at the same speed corresponding to the system mode frequencies, rather it takes place at a lower speed, which depends upon the rate of slowing down of the rotor. The opposite happens during acceleration,

Table 4
Dynamic buckling characteristics of each blade with its root clamped at the top of the disk

Flexural mode	Frequency				Critical compressive buckling load (MN)	
	(a) Stationary		(b) 3000 r.p.m.		(a) Stationary	(b) 3000 r.p.m.
	Non-dimensional frequency parameter ξ	Frequency (Hz)	Non-dimensional frequency parameter ξ	Frequency (Hz)		
First flex	3.5160	42.927	6.7116	81.942	0.1446	0.4892
Second flex	22.0351	269.028	25.8109	315.127	1.3011	1.8937
Third flex	61.7052	753.362	65.6918	802.034	3.6142	4.2267
Fourth flex	120.9317	1476.460	125.1833	1528.369	7.0834	7.7416
Fifth flex	199.9649	2441.380	204.5480	2497.336	11.7098	12.3959
Sixth flex	298.7559	3647.524	302.7786	3696.637	17.4925	18.2613

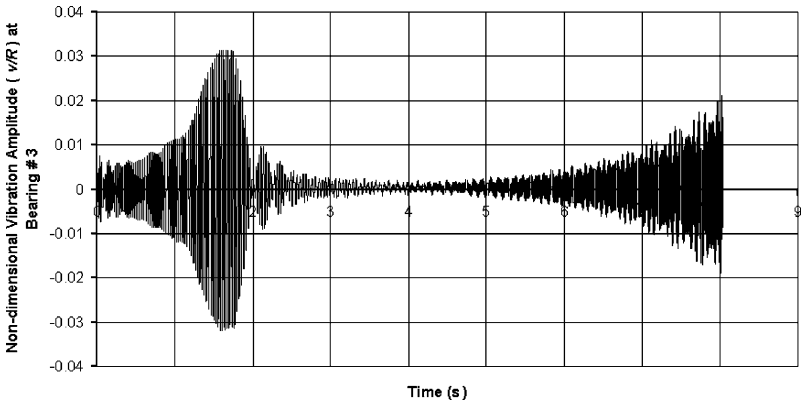

Fig. 8. Analytically computed transient response of a decelerating fan rotor after the blade loss.

where the peak response takes place at a higher speed. This is a generic characteristics of an accelerating and decelerating system as shown by Kammer and Schlack [18].

8. Results and discussion

8.1. Transient dynamic response of the rotor

The rotor model described in Section 7 of this paper is used to study the effect of various parameters affecting the rub load. The effect of varying filler stiffness is highlighted in Fig. 9, where the ratio of the tip clearance of the hard surface to the blade tip radius is kept constant as 0.0467 (Rigid Case Gap = 7 cm, $R = 150$ cm). The rotor radial movement exhibits 2 distinctly different peaks, the first at 450 m/s tip velocity and the second at 370 m/s. The transient radial

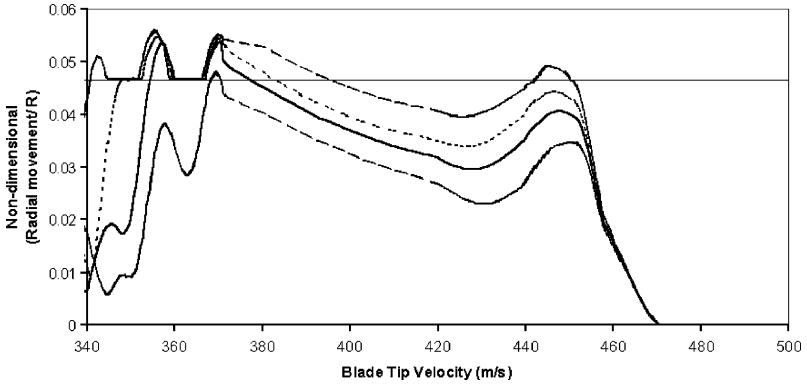

Fig. 9. Non-dimensional radial movement of the center of fan disk after the blade-loss (case filler material thickness/blade tip radius = 0.0467) [———, K_{rub} = 0.0 MN/m (air gap); ……, K_{rub} = 5 MN/m; ———, K_{rub} = 10 MN/m; ————, K_{rub} = 20 MN/m; ——, line for blade tips deforming under hard rub against the rigid fan case].

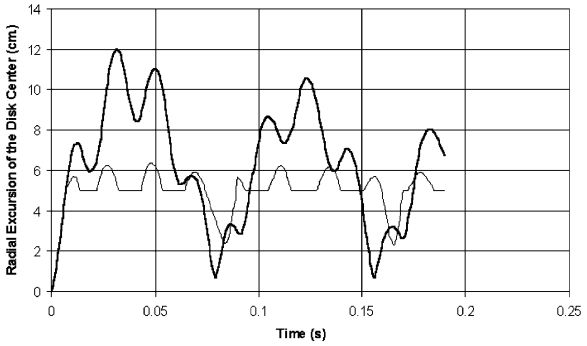

Fig. 10. Transient radial response of the disk center (movement of rotor center beyond 5 cm due to blade tip pulse buckling) with and without the blade rubbing against the fan case after the blade-loss [——, tip clearance = 12 cm; ——, tip clearance = 5 cm].

movement of the rotor is computed for 3 different values of filler material stiffness, namely, 5, 10 and 20 MN/m in addition to the first case with a free air gap and without any filler material in the fan case. The hard rub of blade tip against the outer case would occur at a filler stiffness less than 2 MN/m. During the hard rub, the blade tips deform and the disk center still keeps on moving towards the case. Depending upon the ductility of the blade material the blade tips may plastically curl, or if it is brittle then it may be machined under grinding action. The effect of changing tip clearance is shown in Fig. 10 by plotting the radial movement of the fan rotor after the blade-loss for two different tip clearance values of 5 and 12 cm. The free unimpeded radial movement of the rotor at the disk-center with this much amount of unbalance wants to be 12 cm. Obviously, a tip clearance less than 12 cm would result in the blade tips rubbing against the case, resulting in the dynamic pulse buckling at some critical value of the radial load from the case. For example, with 5 cm of tip clearance the rotor disk-center moves up to 6.5 cm from the center of rotation due to tip buckling of the blade resulting in radial movement of the blade-tip by 1.5 cm. During this

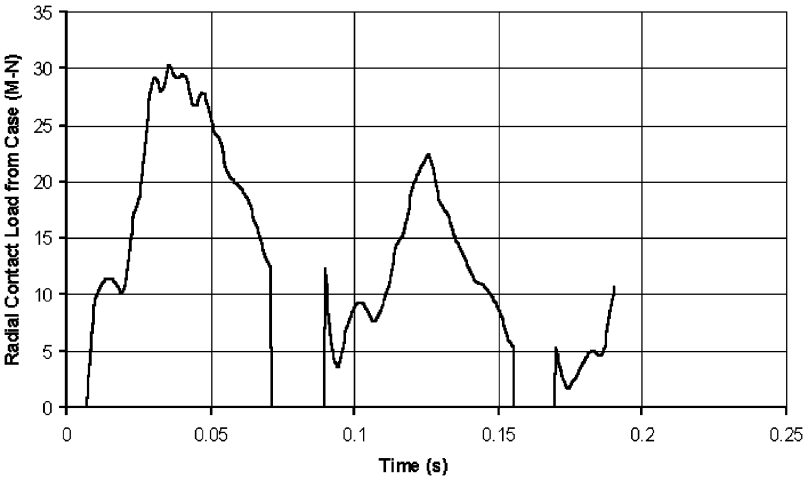

Fig. 11. Transient radial response of the disk center with and without the blade rubbing against the fan case after the blade-loss.

movement of the blade the sum of the radial load from the fan case to the blade tips goes up to 30 MN (see Fig. 11) with first contact lasting for about 0.06 s. It should be noted that this is the analytically computed highest possible radial load on the rotor due to the simplifying assumption of elastic buckling and the blade geometry being completely radial. In reality, the blade tips will deform plastically, once the load is large enough to yield the material and will bend backward easily due to the blade geometry not being completely radial and as such the peak dynamic load in most rub situations will be somewhat lower, but would spread over a longer period than 0.06 s. The instantaneous dynamic stiffness of the rotor during rub changes, but the first elastic contact results in an equivalent blade segment elastic stiffness of 1749 MN/m. However, if the free radial movement of the rotor through the air gap is also taken into account for the effective stiffness calculation, then the numerical value of the effective blade segment elastic stiffness reduces to 190 MN/m. The transient orbit of the fan disk-center after the blade-loss is shown in Fig. 12.

For understanding the effect of changing blade tip clearance on the contact load, the same rotor model was run for the air gap values of 1, 2, 4, 5, 7, 10 and 12 cm. The computed values of peak contact load and the peak radial movement of the rotor in a non-dimensional form as a function of non-dimensional tip clearances are shown in Fig. 13. The plot shows that as the clearance is increased, for a given unbalance of a blade-loss, the radial movement of the rotor increases almost linearly and the contact load decreases with a change in the slope of the curve. From these data, one can compute the effective dynamic stiffness of a segment of rub blades on the rotor during the hard rub as

$$\textit{Effective stiffness} = (\textit{Contact load})/(\textit{Total radial movement of the rotor center} - \textit{tip clearance}).$$

The above relationship is used to plot the curve shown in Fig. 14 from the contact load data of Fig. 13. For most part the blade segment is dynamically more flexible with the increasing clearance. There appears to be a non-dimensional tip clearance value of 0.013 at which the dynamic elastic stiffness value of the blade segment peaks. The peak radial contact load is also

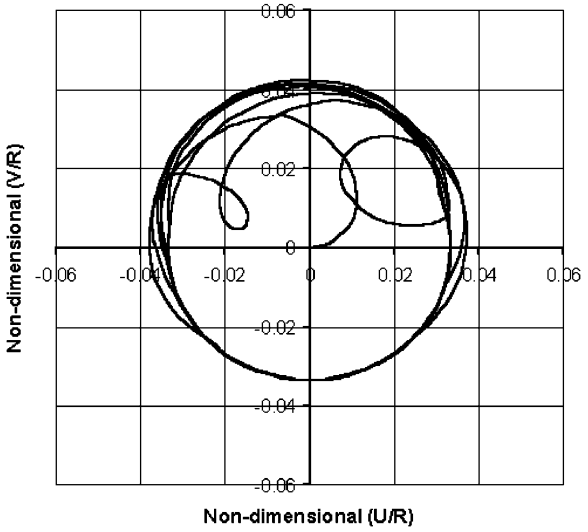

Fig. 12. Non-dimensional orbit of the fan disk center after the unbalance created due to blade loss at 9 o'clock position.

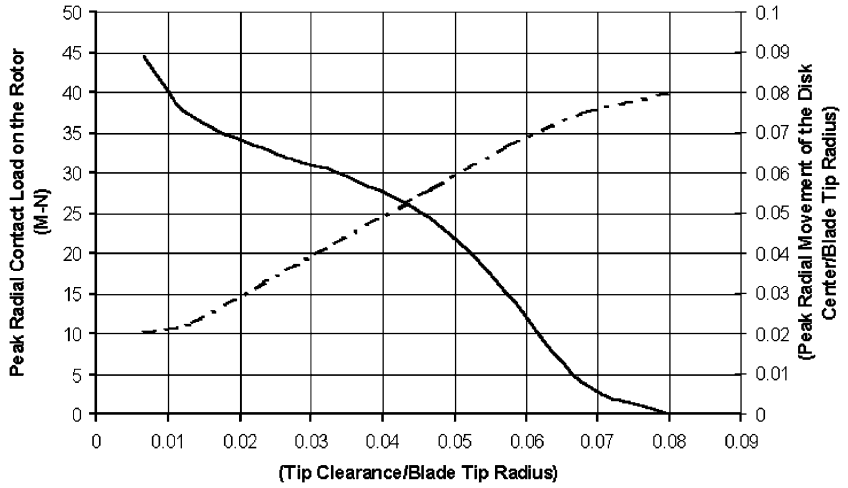

Fig. 13. Peak radial contact load on the rotor and the disk center radial movement as a function of the tip clearance (no filler material) [· — · —, radial movement; ——, contact load].

analyzed for changing stiffness values of the filler material K_{rub}. We have studied its effect for two different values of $K_{rub} = 10$ MN/m and 20 MN/m in addition to free air gap, i.e. $K_{rub} = 0$ (see Fig. 15). As expected, the contact load decreases as the filler material stiffness increases (e.g., for non-dimensional tip clearance of 0.03 the non-dimensional force decreases from 11.5 to 6.5). It is caused because the rotor outward radial velocity during the hard rub decreases, or the rotor is slowed down faster as the filler material gets stiffer.

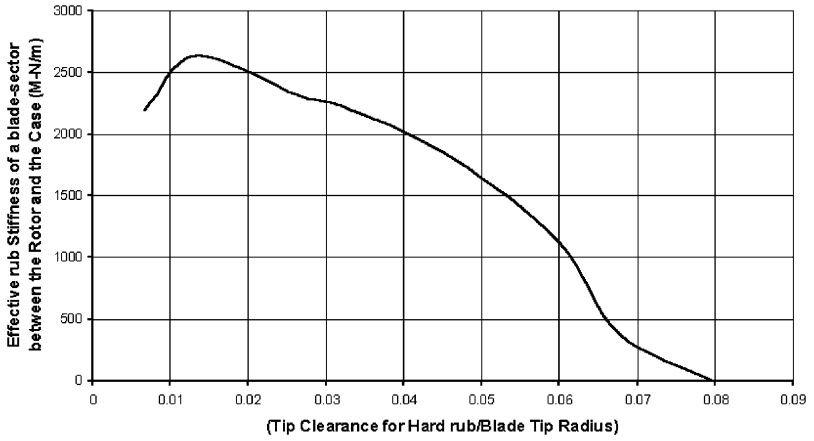

Fig. 14. Effective blade tip rub stiffness between rotor and the case as a function of tip clearance (no filler material).

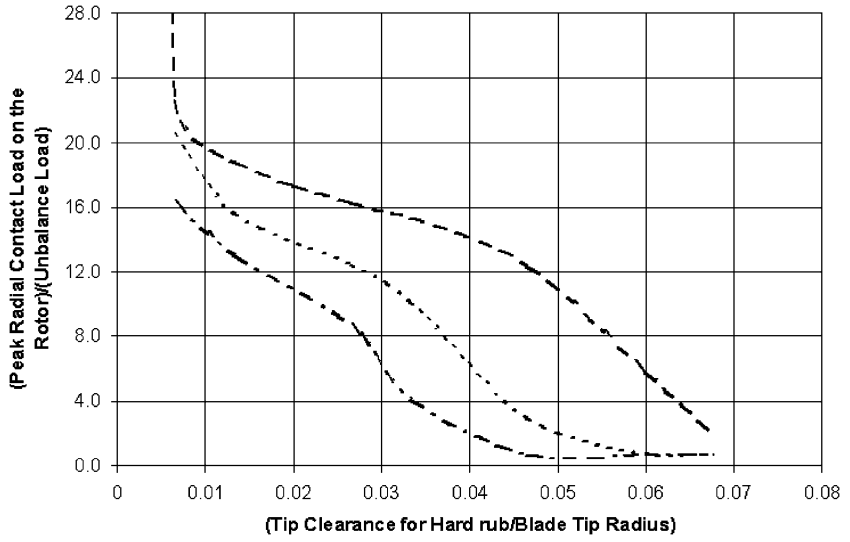

Fig. 15. Non-dimensional peak radial tip rub load on the rotor from the case during hard rub as a function of tip clearance and filler material stiffness [— — — —, air gap $K_{rub} = 0$; ⋯⋯⋯, filler material $K_{rub} = 10$ MN/m; — · — · — · —, filler material $K_{rub} = 20$ MN/m].

The dynamic stability of the same rotor under Coulomb friction has been analyzed for a 360° rub (see Fig. 16). An occasional hard local rub against the case may not be destabilizing. In these situations the rotor can momentarily withstand frictional torque even with a high coefficient of friction. The numerical solution has shown that for an impulse type of torque, the rotor experiences relatively large radial excursion, however it recovers within a few milliseconds and goes to normal steady state rotation. The presence of damping in the bearing support $[\boldsymbol{D}]_b$ matrix plays a significant role in making the system dynamically stable. But, in 360° rub, even a very

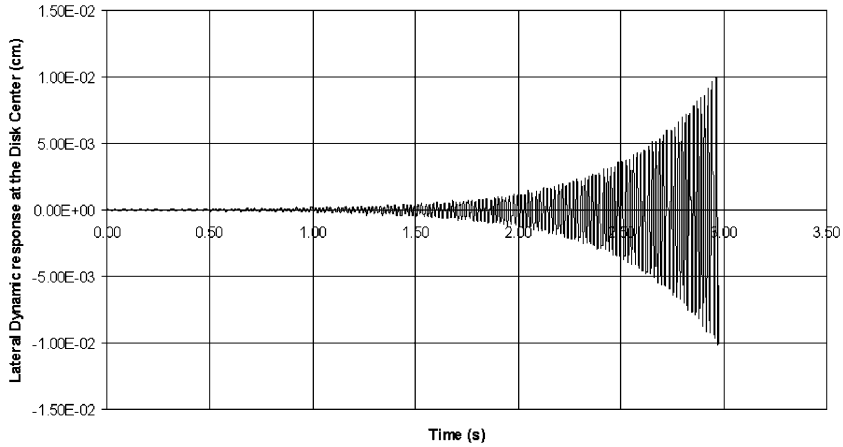

Fig. 16. Dynamic instability developing in a fan rotor with 360° rub with a nominal unbalance (dynamic coefficient of friction at the blade tip $\mu_{dynamic} = 0.01$).

nominal unbalance and a low dynamic coefficient of friction ($\mu_{dynamic} = 0.01$) quickly grows into large radial excursion. In generating the data for Fig. 16, it is assumed that the driving torque is maintaining a constant speed of the rotor. For a given spinning r.p.m. of the rotor, it becomes less stable with increasing torque and more stable with increasing damping.

One of the most interesting observations is that the load torque has much more stabilizing effect at higher speeds on a rotor than a driving torque. As a matter of fact, the rotor becomes stable with the increasing load torque and less stable with the increasing driving torque. An increasing load torque will decelerate the rotor whereas an increasing driving torque will accelerate it. After the blade loss, the frictional torque with the case can cause a very rapid speed drop of the rotor shaft. A correct estimate of transient dynamic load is necessary for the design of the supporting structure.

9. Concluding remark

The paper presents an analytical method to illustrate the non-linear dynamic effect of blades rubbing against the rigid outer case in a rotating machinery. An attempt has been made to quantify the magnitude of the contact load, and it is shown that during the hard rub against the outer case, the sudden impact load can go up by an order of magnitude over the unbalance load. For a typical rotor blade, the radial load from the case to the blade tip can last for 0.05 ms with a peak magnitude reaching up to 30–40 MN. However, it is recognized that the analytically predicted dynamic contact loads in this paper provide an upper bound of the axial load magnitude on the blades due to following two underlying assumptions: (1) Plasticity is not considered and blades remain elastic for the entire duration of impact. (2) Geometrically blades are considered like a cantilever beam of uniform cross-section in the undeformed configuration. Blades are allowed to deform in the lateral direction either due to tangential friction load at the tip, or pulse-buckled deformation under axial impact load.

Due to these two assumptions, the actual contact load will always be lower than computed here for the elastic condition. The method can be refined to take into account the yield stress and elastic–plastic deformation of the blade material. The actual blade cross-section is not a flat plate rather it is made up of an airfoil cross-section, thick in the middle and thin at the lead and trail edges. Furthermore, the typical blade is not straight radial either, rather it is twisted as one moves from the root of the blade at the disk-top to the tip of the blade. The current method can be extended further to consider more realistic geometrical representation of the blade by simply replacing the blade stiffness terms for a twisted and curved beam, which can be derived easily as shown by the author earlier [34].

In addition, a locally rubbing blade tip can be considered under Hertzian contact, which is non-linear in nature. In the present analysis, the blade is considered to deform due to lateral buckling, but the local deformation is neglected. During the hard-rub against the fan case, the contact loading is very similar to Hertzian contact, where the contact force F_{case} is proportional to the blade tip radial-deflection δ such that

$$F_{case} = K_{rub}(\delta)^{3/2}.$$

Appendix A. Nomenclature

a_k, b_k	time-independent Fourier coefficients
$(A)_s$	cross-sectional area of shaft $= \pi(r_o^2 - r_i^2)$
$(A)_b$	cross-sectional area of the blade
$\boldsymbol{B}_1$	time-dependent stiffness matrix (symmetrical due to axial load on the shaft)
$\boldsymbol{B}_2$	time-dependent stiffness matrix (skew-symmetric due to fluctuating torque in the system)
$\boldsymbol{C}_D$	damping matrix (symmetrical or non-symmetrical depending upon the bearing)
$\boldsymbol{C}_G$	gyroscopic matrix (skew-symmetric, causes forward and backward whirl in the shaft)
c	blade chord length at the tip
$\boldsymbol{C}$	general damping matrix
C_c	critical damping parameter (viscous) in the blade
C_t	value of dash-pot viscous damping at the blade tip
$[C_{i,j}]$	a typical ith row and jth column term in the velocity-dependent matrix
D_L	axial length of the rigid disk
$D^b_{xx}, D^b_{xy}..$	damping in the bearing support
e	non-dimensional factor used to linearize the effect of blade rotation
$(EI)_s$	flexural rigidity of the rotor shaft
$(EI)_b$	flexural rigidity of the blade
F_a	axial load on the blade (in the global radial direction)
F_G	gas load perpendicular to the blade pressure surface on each blade
F_U	$m_r\Omega^2$
$\boldsymbol{F}(t)$	column vector containing external forces on the dynamical system
$\boldsymbol{f}(t)$	column vector containing generalized co-ordinates of the dynamical system

$f_n(t)$	nth term of the time-dependent generalized co-ordinates (length unit)
H	critical damping parameter in the shaft
I_d	diametral mass moment of inertia of the shaft (per unit length) $= (\rho A)_s(r_o^2 + r_i^2)/4$
I_p	polar mass moment of inertia of the rotor shaft (per unit length) $= 2I_d$
J	diametral mass moment of inertia of the disk and all N-blades
J_D	diametral mass moment of inertia of the disk
K_{rub}	radial stiffness of the outer case filler material during rub
K_{shaft}	lateral stiffness of the shaft at the disk center
$\boldsymbol{K}$	general stiffness matrix
$\boldsymbol{K}_S$	stiffness matrix (generally symmetrical, but may be non-symmetrical due to non-symmetrical bearing in the horizontal and vertical directions)
$\boldsymbol{K}_I$	instability matrix (skew-symmetric caused by the internal damping in the shaft and also torque in the system)
$[K_{i,j}]$	a typical ith row and jth column term in the stiffness matrix
L	span length of the cantilever blade
ℓ	span length of the shaft
$\boldsymbol{M}$	mass matrix (symmetrical)
$[M_{i,j}]$	a typical ith row and jth column term in the mass matrix
M_D	mass of the disk only
M_b	mass of each blade $= (\rho A)_b L$
M	mass of the disk and all N-blades $= M_D + N(\rho A)_b L$
m_r	mass moment of unbalance
N_b	number of discrete bearings supporting the shaft
N_c	number of diametral modes in the casing
N	number of blades on the rotor
P_0	steady state axial load on the shaft
P_t	time-dependent axial load on the shaft
$P(t)$	axial force due to gas load on blade and rotating unbalance of F_U (+ sign: tension or, − sign: compression). For large disk movement, this axial force on the shaft is highly non-linear and the cone angle in the containment ring also produces an axial load component $= NF_G \sin\beta + u_{,z}[F_U \cos(\theta+\phi) - (\cos\varphi - \mu\sin\varphi)F_{case}] + v_{,z}[F_U \sin(\theta+\phi) - (\sin\varphi + \mu\cos\varphi)F_{case}]$
$q_x(z,t)$	$[F_U \cos(\theta+\phi) - (\cos\varphi - \mu\sin\varphi)F_{case}]\delta(z-\ell)$
$q_y(z,t)$	$[F_U \sin(\theta+\phi) - (\sin\varphi + \mu\cos\varphi)F_{case}]\delta(z-\ell)$
R	blade tip radius
r	blade root radius = disk outer radius
$\boldsymbol{P}, \boldsymbol{Q}$ and $\boldsymbol{R}$	matrices in the ascending powers of λ
s	blade local co-ordinates in the global direction
S^b_{xx}, S^b_{xy}..	stiffness in the bearing support
$T(t)$	torque due to gas load on the blade and tip rub friction (torque has + sign for a driving torque that is in the direction of rotation, and has − sign for the direction opposite to the rotation) $= -NF_G(r + 0.5L)\cos\beta - \mu R F_{case}$
T_0	steady state torque on the shaft

T_t	time-dependent torque on the shaft
$u(z,t)$	transient deflection of the shaft in the global x direction
$U_m(t)$	time-dependent generalized co-ordinates for deflection of the shaft (x direction)
$v(z,t)$	transient deflection of the shaft in the global y direction
$V_m(t)$	time-dependent generalized co-ordinates for deflection of the shaft (y direction)
$W_m(z)$	displacement function or mode shapes of the rotor shaft
$X_0(t), X_1(t),...$	time-dependent generalized co-ordinates for dynamic deflection of the blade
$Y_n(s)$	displacement function or mode shapes of the cantilever blades
z	axial co-ordinate of a point on the shaft

Greek letters

β	blade stagger angle (radian) i.e., angle between the blade chord and the engine axis (axis of rotation) at the blade tip
δ	effective logarithmic decrement as a measurement of damping
$\delta(z-z_i)$	Dirac Delta function for $z=z_i$
ε	radial incursion of the blade tip in the case filler material during rub (interference)
ζ_b	non-dimensional damping factor for the blade material
$\eta(s,t)$	lateral deflection of the blade
θ	angle of the rigid body rotation of the shaft about the spin axis at time 't' from time '0' ($\theta=\Omega t$ for constant angular velocity 'Ω')
λ	eigenvalues
λ_r, λ_i	real and imaginary parts of the eigenvalue
μ	dynamic coefficient of friction between the blade tip and the outer case
ξ	non-dimensional beam frequency parameter
$(\rho)_c$	mass density of the case filler material
$(\rho)_s$	ρ_{shaft} (mass density of the shaft material)
τ	ultimate shear strength of the case filler material
ϕ	circumferential location of unbalance at time 't' $=0$ (constant)
φ	angle of the shaft center eccentricity in the fixed frame of reference during the blade tip rub with the case (a function of time 't')
ψ	phase difference
$\Re(u,v)$	differential operator
ω_n	natural frequency (rad/s)
Ω	rotor spin velocity (rad/s) $=(\mathrm{d}\theta/\mathrm{d}t)$

Subscripts

b	refers to material and cross-section data with respect to the blade
i,j	refers to ith row and jth column term of the respective matrix
j	refers to a typical jth blade in a cascade of N-blades
k	refers to a typical term in Fourier series
m	refers to number of modes on the shaft
n	refers to number of modes on the blade

q refers to a typical term in Fourier series
s refers to material and cross-section data with respect to the shaft

References

[1] J.C. Snowdon, *Vibration and Shock in Damped Mechanical Systems*, Wiley, New York, 1968, pp. 333–365.
[2] D.J. Inman, A.N. Andry Jr., Some results on the nature of eigenvalues of discrete damped linear systems, *American Society of Mechanical Engineers, Journal of Applied Mechanics* 47 (1980) 927–930.
[3] M. Ahmadian, S.H. Chou, A new method for finding symmetric form of asymmetric finite-dimensional dynamic systems, *American Society of Mechanical Engineers, Journal of Applied Mechanics* 54 (1987) 700–705.
[4] R.H. Plaut, Stability of rotating shafts with axial load and damping, in: R.N. Dubey, N.C. Lind (Eds.), *Proceedings of the First ASCE-EMD Specialty Conference on Mechanics in Engineering*, University of Waterloo Press, Waterloo, Canada, 1977, pp. 133–148.
[5] R. Cohen, I. Porat, Coupled torsional and transverse vibration of unbalanced rotor, *American Society of Mechanical Engineers, Journal of Applied Mechanics* 52 (1985) 701–705.
[6] K.B. Yim, S.T. Noah, J.M. Vance, Effect of tangential torque on the dynamics of flexible rotors, *American Society of Mechanical Engineers, Journal of Applied Mechanics* 53 (1986) 711–718.
[7] S.K. Sinha, On general conditions of rotordynamic stability under combined axial forces and torque, *American Society of Mechanical Engineers, Journal of Applied Mechanics* 59 (1992) 225–228.
[8] C.W. Lee, J.S. Yun, Dynamic analysis of flexible rotors subjected to torque and force, *Journal of Sound and Vibration* 192 (2) (1996) 439–452.
[9] D.W. Child, Rub induced parametric excitation in rotors, *American Society of Mechanical Engineers, Journal of Mechanical Design* 10 (1979) 640–644.
[10] A. Sinha, J.H. Griffin, Effects of static friction on the forced response of frictionally damped turbine blades, *American Society of Mechanical Engineers, Journal of Engineering for Gas Turbines and Power* 106 (1) (1984) 65–69.
[11] A. Sinha, Friction damping of random vibration in gas turbine engine airfoils, *International Journal of Turbo and Jet Engines* 7 (1990) 95–102.
[12] J.H. Wang, W.L. Shieh, The influence of variable friction coefficient on the dynamic behavior of a blade with friction damper, *Journal of Sound and Vibration* 149 (1991) 137–145.
[13] K.Y. Sanliturk, M. Imregun, D.J. Ewins, Harmonic balance vibration analysis of turbine blades with friction dampers, *American Society of Mechanical Engineers, Journal of Vibration and Acoustics* 119 (1997) 96–103.
[14] E.J. Berger, M.R. Begley, M. Mahajani, Structural dynamic effects on interface response—formulation and simulation under partial slipping conditions, *American Society of Mechanical Engineers, Journal of Applied Mechanics* 67 (2000) 785–792.
[15] F.K. Choy, J. Padovan, Non-linear transient analysis of rotor-casing rub events, *Journal of Sound and Vibration* 113 (3) (1987) 529–545.
[16] F.K. Choy, J. Padovan, C. Batur, Rub interactions of flexible casing rotor systems, *Journal of Engineering for Gas Turbines and Power* 111 (4) (1989) 652–658.
[17] F.K. Choy, J. Padovan, W.H. Li, Rub in high performance turbo-machinery, modeling, solution methodology and signature analysis, *Mechanical Systems and Signal Processing* 2 (2) (1988) 113–133.
[18] D.C. Kammer, A.L. Schlack Jr., Effects of non-constant spin rate on the vibration of a rotating beam, *American Society of Mechanical Engineers, Journal of Applied Mechanics* 54 (1987) 305–310.
[19] D.J. Segalman, C.R. Dohrmann, A method for calculating the dynamics of rotating flexible structures (part 1: derivation, part 2: example calculations), *American Society of Mechanical Engineers, Journal of Vibration and Acoustics* 118 (3) (1996) 313–322.
[20] D.C.D. Oguamanam, G.R. Heppler, Geometric stiffening of Timoshenko beams, *American Society of Mechanical Engineers, Journal of Applied Mechanics* 65 (1998) 923–929.
[21] S.M. Lin, Dynamic analysis of rotating non-uniform Timoshenko beams with an elastically restrained root, *American Society of Mechanical Engineers, Journal of Applied Mechanics* 66 (1999) 742–748.

[22] H.E. Lindberg, A.L. Florence, *Dynamic Pulse Buckling*: *Theory and Experiment*, Martinus Nijhoff, Dordrecht, 1987, pp. 2–73.
[23] D.R. Chivens, H.D. Nelson, The natural frequencies and critical speeds of a rotating, flexible shaft–disk system, *American Society of Mechanical Engineers, Journal of Engineering for Industry* 97 (1975) 881–886.
[24] C.W. Lee, R. Katz, A.G. Ulsoy, R.A. Scott, Modal analysis of a distributed parameter rotating shaft, *Journal of Sound and Vibration* 122 (1988) 119–130.
[25] S.M. Yang, G.J. Sheu, Vibration control of a rotating shaft: an analytical solution, *American Society of Mechanical Engineers, Journal of Applied Mechanics* 66 (1999) 254–259.
[26] R.G. Parker, Analytical vibration of spinning, elastic disk-spindle systems, *American Society of Mechanical Engineers, Journal of Applied Mechanics* 66 (1999) 218–224.
[27] C.W. Lee, Y.G. Jei, Modal analysis of continuous rotor-bearing systems, *Journal of Sound and Vibration* 126 (2) (1988) 345–361.
[28] Y.G. Jei, C.W. Lee, Modal analysis of continuous asymmetrical rotor-bearing systems, *Journal of Sound and Vibration* 152 (2) (1992) 245–262.
[29] N. Khader, Stability analysis for the dynamic design of rotors, *Journal of Sound and Vibration* 207 (3) (1997) 287–299.
[30] T. Zheng, N. Hasebe, Nonlinear dynamic behaviors of a complex rotor-bearing system, *American Society of Mechanical Engineers, Journal of Applied Mechanics* 67 (2000) 485–495.
[31] S.K. Sinha, Stability of viscoelastic rotor–disk system under dynamic axial loads, *AIAA Journal* 27 (1989) 1653–1655.
[32] P. Pedersen, A.P. Seyranian, Sensitivity analysis for problems of dynamic stability, *International Journal of Solids and Structures* 19 (4) (1983) 315–335.
[33] C.M. Harris, C.E. Crede, *Shock and Vibration Handbook*, 2nd Edition, McGraw-Hill, New York, 1976, pp. 7–14.
[34] S.K. Sinha, On a general method of vibration analysis in curvilinear coordinates, *AIAA Journal* 26 (1988) 629–631.